

Numerical Simulations and Coarse-Graining

Fernando F. Grinstein

Abstract

Accurate predictions with quantifiable uncertainty are essential to many practical turbulent flows in engineering, geophysics, and astrophysics typically comprising extreme geometrical complexity and broad ranges of length and timescales. Dominating effects of the flow instabilities can be captured with coarse-graining (CG) modeling based on the primary conservation equations and effectively codesigned physics and algorithms. The collaborative computational and laboratory experiments unavoidably involve inherently intrusive coarse-grained observations – intimately linked to their subgrid scale and supergrid (initial and boundary conditions) specifics. We discuss turbulence fundamentals and predictability aspects and introduce the CG modified equation analysis. Modeling and predictability issues for underresolved flow and mixing driven by underresolved velocity fields and underresolved initial and boundary conditions are revisited in this context. CG simulations modeling prototypical shock-tube experiments are used to exemplify relevant actual issues, challenges, and strategies.

1.1 Introduction

Mixing of initially separate materials by turbulent motions is a critical element in many research areas of interest, such as inertial confinement fusion, combustion, and supernova implosions and explosions, where vorticity is introduced at material interfaces by (interface) acceleration or impulsive loading of shock waves, and turbulence is generated via flow instabilities (Zhou, 2017a,b). Hydrodynamics of interest depends on initial conditions and involves transition to turbulence, nonequilibrium turbulence development, and late-time relaminarization. Flow instabilities and associated vortex production driving high Reynolds number (Re) mixing are crucial ingredients in the enstrophy budget equation,

$$\begin{aligned}
 D\Omega/Dt \sim & \underbrace{\{\omega_i s_{ij} \omega_j\}}_{\text{(a) vortex stretching}} + \underbrace{\{\omega_i \omega_j\} S_{ij}}_{\text{(b) KH, Dilatational, BP, \dots}} \\
 & + \underbrace{\epsilon_{ijk} \bar{\rho}^{-2} \{\omega_i \rho_{,j}\} P_{,k}}_{\text{(c) Baroclinic: RT, RM, \dots}} + \underbrace{\epsilon_{ijk} \bar{\rho}^{-2} \{\omega_j p_{,i}\} \rho_{,k}}_{\text{(d) other Baroclinic \dots}} + \text{viscous terms,}
 \end{aligned} \tag{1.1}$$

where mean enstrophy $\Omega = \{\omega_i \omega_i\}$ is defined in terms of the vorticity components ω_i , P is mean pressure, s_{ij} and S_{ij} are fluctuating and mean strain rates, $s_{ij} = (u_{i,j} + u_{j,i})/2$, $\bar{\rho}$ is mean mass density, and the brackets $\{\}$ denote ensemble averaging.

Highlighted terms on the right-hand side of equation (1.1) depict *inherently inviscid* instability mechanisms governing the high Re regimes: (a) vortex stretching driving vortex cascade and transition to turbulence – only present in 3D; (b) mean-shear driven Kelvin–Helmholtz (KH) instability, mean dilatation by shock and the Bell–Plesset (BP) convergence instability; (c) two baroclinic instabilities proportional to pressure gradients – *one* corresponding to the classical Richtmyer–Meshkov (RM) and Rayleigh–Taylor (RT) drivers; and (d) two other baroclinic instabilities proportional to density gradients.

Laboratory studies typically demonstrate the end outcome of complex, nonlinear, three-dimensional physical processes with many unexplained details and mechanisms. Flow experiments based on numerical simulations carried out with precise control of initial and boundary conditions are ideally suited to provide insights into the underlying dynamics of the laboratory observations. Direct numerical simulation (DNS) – capturing the dynamics of all relevant space/timescales of motion without any turbulence model, typically based on the numerical solution of the continuum Navier–Stokes equations (NSE), is prohibitively expensive in the foreseeable future for practical flows of interest at moderate-to-high Re . At the other end of the simulation spectrum are the Reynolds averaged Navier–Stokes equations (RANS) approaches, which solve flow equations averaged over time, spatially homogeneous directions, or across an ensemble of equivalent flows, and model mean flow effects.

Alternatively, the coarse-graining (CG) paradigms presume the spectral cascade rate of energy (the rate-limiting step) is determined by the initial and boundary conditions constrained large-scale dynamics – which enslaves the small-scale flow dynamics. Small-scale assumptions are the basis for a variety of CG turbulence approaches, all assuming that turbulence can be split into two groups: one consisting of the resolved geometry and regime-specific scales – the so-called energy-containing scales; the other associated with the unresolved smallest eddies, for which presumably more-universal flow dynamics is represented with subgrid scale (SGS) closure models. CG strategies include classical large eddy simulation (LES, Sagaut et al. 2006), focusing on explicit use of SGS closure models, implicit LES (ILES, Grinstein et al. 2010), relying on SGS modeling and filtering provided by physics capturing numerical algorithms, and hybrid RANS/LES bridging approaches (Frolich and von Terzi, 2008).

In practice, all simulation models reduce the range of reduced scales. Both CG simulations and DNS (as practiced) presume scale separation between resolved and unresolved scales to be possible – DNS leaves out the longest scales (e.g., through periodicity constraints) and CG simulations model the effects of the shortest scales. RANS typically presumes equilibrium developed turbulence – and thus models effects of *all* scales. Realizability in capturing *questions and quantities of interest* are the only solid basis to establish simulation model adequacy and effectiveness – there is no *absolutely better* ranked simulation model¹ and a suitable set of modeling ingredients for the prediction task at hand must be prescribed.²

¹ *Essentially, all models are wrong, but some are useful* (Box, 1979).

² *Everything should be made as simple as possible, but no simpler* – attributed to Albert Einstein.

Computation of *quantities of interest* requires building appropriate physics in the actual equations solved as the basis of the simulation model and a suitable verification, validation, and uncertainty quantification framework. Predictability issues in the collaborative laboratory/computational context involve characterizing and modeling the relevant flow conditions at the SGS level – within a computational cell *or* instrumentation resolution, and at the supergrid (SPG) scale – at initialization and boundaries of computational *and* laboratory experiments.

1.2 Turbulence Modeling and Predictability

Outstanding fundamental open questions in the turbulence modeling context have been usefully delineated by Tsinober (2009, 2011): *Why modeling works? Models versus physical laws / first principles, or Models versus physics and mathematics in turbulence? What is the meaning of the term ‘works’? What is the meaning of experimental validation of models? Can models clarify the physics and produce genuine predictions, or are they just a ‘kind’ of ‘postdiction’ and sophisticated methods of data description/fitting?*

Emulating particular flow realizations demands SPG choices at initialization and boundaries of computational *and* laboratory experiments (Grinstein, 2004). Long-term effects of SPG specifics have been extensively observed in the laboratory experiments (Hussain and Zedan, 1978; Gutmark and Ho, 1983; Wignanski et al., 1986; George, 1990; Li and Gutmark, 2006). The crucial SPG issues were clearly recognized by George (1990): *Unlike the theoretician, the experimentalist already knows the solution, for it is the flow he has realized. His objective is to find which equations and which boundary and initial conditions his solution corresponds to and then to compare them and his results to those dealt with by the theoretician.*

The sensitivity of turbulent flows to initial conditions is now well established. Far-field (and late time) characteristics of turbulent flows remember their near-field (and initial) features (Wignanski et al., 1986; George, 1989; Slessor et al., 1998; Ramaprabhu et al., 2005), and the mechanism by which transition from initial conditions to asymptotic flow occurs involves unsteady large-scale coherent structure dynamics; transition can be captured by CG simulations but not by single-point closure modeling (George and Davidson, 2004b; George and Tutkun, 2009) typical in RANS. The long-standing view that initial conditions independent universal turbulence state are achieved in the far field (or at late times) – for example, Townsend (1976) – has been replaced by the recognition that *different self-similar end turbulence states are possible depending on initial conditions* (George, 1989).

Computational and laboratory observations are inherently intrusive due to characterization and modeling uncertainties – versus nature’s separate physics control. Suitable modeling, computational design, and initial conditions characterization and parameterization must be combined within appropriate validation and uncertainty quantification frameworks *to ensure repeatability of computational and laboratory experiments for the predictability assessments* – Figure 1.1³.

³ *What we observe is not nature itself but nature exposed to our method of questioning. Our scientific work in physics consists of asking questions about nature in the language that we possess and trying to get an answer from experiments by the means that are at our disposal* (Heisenberg, 1958).

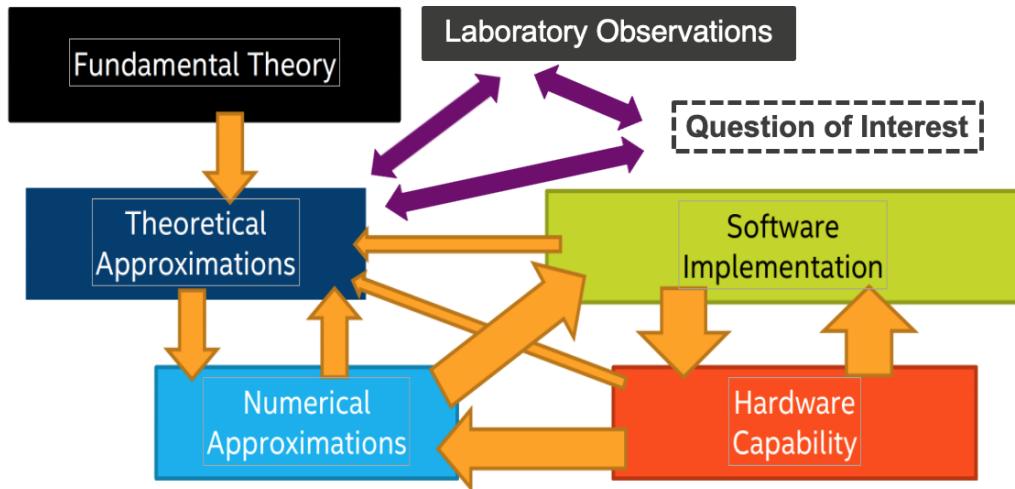


Figure 1.1 Predictions are constrained by strong interactions between closely coupled models, theory, laboratory observations, theoretical and numerical approximations, software implementation, and hardware capability.

1.3 Low-Pass Filtered and Discretized Navier–Stokes Equations

To simplify discussion and conceptualization, Sections 1.3–1.3.1 focus on a continuum formulation of incompressible flow with scalar mixing – exemplifying issues and challenges with coupled physics of frequent interest.

Turbulent mixing of material scalars can be usefully characterized by the length scales of the fluid physics involved: (1) large-scale entrainment in which advection brings relatively large regions of the pure materials together; (2) an intermediate length scale associated with the convective stirring due to velocity gradient fluctuations; and (3) much smaller scale interpenetration resulting from molecular diffusion. At moderate and high Re – when convective timescales are much smaller than those associated with molecular diffusion – and for Schmidt number $Sc \sim 1$, large-scale vortices and their interactions play a crucial role in controlling transitional growth and entrainment, and the primary concern is with the numerical simulation of the first two processes above – advection and stirring.

CG simulations involve solving the NSE with the smallest resolved length scale fixed by a characteristic filter length – based on available physics insights on the problem of interest and on which results depend. Equations for the filtered unknowns follow from applying a spatial filtering operation to velocity and mixing scalar equations,

$$\frac{\partial \bar{u}_i}{\partial t} + \frac{\partial (\bar{u}_i \bar{u}_j)}{\partial x_j} + \frac{1}{\rho} \frac{\partial \bar{p}}{\partial x_i} - \nu \left(\frac{\partial^2 \bar{u}_i}{\partial x_j \partial x_j} \right) = -\frac{\partial}{\partial x_i} (\nabla \cdot \tau_{\mathbf{u}} + \phi_{\mathbf{u}}), \quad (1.2)$$

$$\frac{\partial \bar{c}}{\partial t} + \frac{\partial (\bar{c} \bar{u}_j)}{\partial x_j} - \mathcal{D}_s \left(\frac{\partial^2 \bar{c}}{\partial x_j \partial x_j} \right) = -\nabla \cdot \tau_c + \phi_c, \quad (1.3)$$

where overbars denote the filtering operation $\bar{q} = \int q(\mathbf{x}')G(\mathbf{x}', \mathbf{x})dx'dy'dz'$ characterized by a generic prescribed kernel $G(\mathbf{x}', \mathbf{x})$. Moreover, \mathbf{u} is the (here presumed solenoidal) velocity field, c is a conserved material scalar concentration, p is the pressure, ν and \mathcal{D}_s denote viscosity and scalar diffusivity, respectively, $\tau_{\mathbf{u}} = \overline{\mathbf{u} \otimes \mathbf{u}} - \bar{\mathbf{u}} \otimes \bar{\mathbf{u}}$ and $\tau_c = \overline{c \mathbf{u}} - \bar{c} \bar{\mathbf{u}}$ are explicit SGS models needed to close the equations in filtered unknowns. Finally, $\phi_{\mathbf{u}}$ and ϕ_c are terms due to potential noncommuting differentiation and filtering – typically lumped together with the prescribed explicit SGS models $\tau_{\mathbf{u}}$ and τ_c .

As inverse filtering operations are necessarily ill-posed, we estimate $\tau_{\mathbf{u}}$ and τ_c through approximate inversion, for example, for $\tau_{\mathbf{u}}$ – after discretization $\mathbf{u} \rightarrow \mathbf{u}_n$,

$$\tau_{\mathbf{u}}^n = \underbrace{(\mathbf{u} \otimes \bar{\mathbf{u}} - \mathbf{u}_n \otimes \bar{\mathbf{u}}_n)}_{\text{stress model}} + \underbrace{(\bar{\mathbf{u}}_n \otimes \mathbf{u}_n - \bar{\mathbf{u}}_n \otimes \bar{\mathbf{u}}_n)}_{\text{grid resolved stress}}, \tag{1.4}$$

where $\tau_{\mathbf{u}}$ is thus formally decomposed in terms of modeled and grid-resolved components – for example, von Kaenel et al. (2003). Hard deconvolution is associated with the continuum-grid link portion, approximately accounting for grid nonrepresented information, which must be necessarily modeled. Softer deconvolution involves seeking approximations associated with grid-represented scales.

1.3.1 Modified Equation Analysis of Coarse-Graining

Formal CG simulations analysis can be based on modified equation analysis (Hirt, 1969; Ghosal, 1996), a technique for generating approximate equations for the computed solutions – actual solutions of the numerical algorithm underlying the simulation model. A detailed discussion of modified equation analysis for LES, including compressibility, has been presented separately (Fureby and Grinstein, 1999; Margolin and Rider, 2010; Grinstein and Fureby, 2007).

The modified equations satisfied by the computed numerical solutions with the given discretization method have the general form,

$$\frac{\partial \bar{u}_i}{\partial t} + \frac{\partial (\bar{u}_i \bar{u}_j)}{\partial x_j} + \frac{1}{\rho} \frac{\partial \bar{p}}{\partial x_i} - \nu \frac{\partial^2 \bar{u}_i}{\partial x_j \partial x_j} = - \frac{\partial}{\partial x_i} (\nabla \cdot \tau_{\mathbf{u}} + \phi_{\mathbf{u}} + t_{\mathbf{u}}), \tag{1.5}$$

$$\frac{\partial \bar{c}}{\partial t} + \frac{\partial (\bar{c} \bar{u}_j)}{\partial x_j} - \mathcal{D}_s \frac{\partial^2 \bar{c}}{\partial x_j \partial x_j} = - \nabla \cdot \tau_c + \phi_c + t_c, \tag{1.6}$$

where the new terms on the right, $t_{\mathbf{u}}$ and t_c , denote implicit SGS models associated with discretization truncation.

High Re turbulent flow physics can be captured with CG simulations (Grinstein, 2016). Depending on the simulation model equations solved – and actual values of Re and other characteristic (e.g., Schmidt, Damkohler, Knudsen) numbers, combined explicit and implicit SGS models may be needed to address physics such as diffusive mixing and combustion, as well as noncontinuum statistical aspects. *In the absence of an established universal theory of turbulence, the construction of SGS models is pragmatic and primarily based on rational use of empirical information.*

Convergence issues versus resolution in turbulent flow simulations are typically problem-dependent and difficult to address in general. Grid independence can be, in principle, achieved

with DNS. Otherwise, inherent to any CG approach is the fact that the smallest resolved turbulence scale is determined by the resolution cutoff wavelength prescribed by explicit or implicit spatial filtering. Ideally, the CG smallest resolved length scale is fixed by a chosen characteristic grid-independent filter length – for example, Bose et al. (2010), on which results are still dependent. However, as computational resolution requirements become prohibitively expensive for problems involving complex flow and geometries at moderate-to-high Re , well-established practical CG typically relies on the implicitly provided discretization filtering – for example, Hill et al. (2006).

Implicit Large Eddy Simulation

The question of whether LES is a physical model, a numerical procedure, or a combination of both has been discussed in detail by Pope (2004). The crucial practical computational aspect is the need to distinctly separate (and effectively combine) the effects of explicit spatial filtering and SGS reconstruction models from their unavoidable implicit counterparts due to discretization – which have been demonstrated to be comparable in the classical LES practice (Ghosal, 1996).

Given the seemingly insurmountable issues posed to LES by underresolution, the possibility of relying on the SGS modeling and filtering provided implicitly by the numerical algorithms was proposed as an option (Boris, 1990; Boris et al., 1992; Fureby and Grinstein, 1999). From the modified equation analysis perspective, the crucial caveat is that good or bad SGS physics can be built into a (so-called) *no-model simulation model* depending on numerical schemes and their particular spatiotemporal implementation.

Many numerical paradigms have been proposed in the ILES context, including nonoscillatory finite-volume algorithms – surveyed in Grinstein et al. (2010), spectral viscosity vanishing methods (Karamanos and Karniadakis, 2000), approximate deconvolution (Stolz et al., 2001; Domaradzki and Adams, 2002), vorticity confinement (Fan et al., 2002), combined compact differencing and filtering (Visbal and Rizzetta, 2002), weighted essentially nonoscillatory methods (Schilling and Latini, 2010), discontinuous Galerkin (Uranga et al., 2011), and finite elements (Wang et al., 2021).

Underresolved simulations are typically unavoidable in the high Re turbulent flow applications at scale, and ILES often becomes the effective CG strategy to capture the dominating effects of flow instabilities. Comparisons of instantaneous probability distribution functions of explicit and implicit SGS viscosities for homogeneous isotropic turbulence showed similar behaviors dependent on the actual SGS models involved (Fureby and Grinstein, 1999). Well-behaved ILES spectral eddy viscosities in agreement with theory (Domaradzki et al., 2003; Thornber et al., 2007) were also reported. Positive evaluations of ILES of forced and decaying isotropic turbulence have been reported (Porter et al., 1998; Fureby and Grinstein, 2002; Domaradzki et al., 2003; Margolin et al., 2006; Thornber et al., 2007; Grinstein, 2020). Turbulent mixing of a passive scalar by forced isotropic turbulence with a prescribed mean scalar gradient (Wachtor et al., 2013) as function of effective turbulence Re determined by grid resolution showed that a properly designed ILES can accurately capture the asymptotic behaviors of high Re *stirring-driven* turbulent mixing associated with the mixing transition (Dimotakis, 2000). ILES based on effectively codesigned physics and numerical models solving the compressible conservation equations with nonoscillatory finite-volume algorithms have been used to study transition to turbulence from laminar conditions in free

shear flows; the occurrence of global instabilities, complex dynamics of three-dimensional vortical geometries, and their impact on jet entrainment and combustion have been surveyed separately (Grinstein, 2001, 2010).

The monotone integrated LES (MILES) approach (Boris, 1990; Boris et al., 1992) incorporates the effects of the SGS physics on the resolved scales through functional reconstruction of the convective fluxes using locally monotonic finite-volume schemes. The more broadly defined ILES in Grinstein et al. (2010) focused on using nonoscillatory finite-volume algorithms to solve the unfiltered Euler or NSE, such as the flux-corrected transport, the piecewise parabolic method, the multidimensional positive definite advection transport algorithm, Godunov, and total variation diminishing algorithms.

By concentrating on resolving the inertially dominated flow dynamics and the regularization of underresolved flow, ILES follows on the precedent of using nonoscillatory finite-volume methods for shock capturing – requiring weak solutions and satisfying an entropy condition. In apparent serendipity, physics built over decades into popular nonoscillatory finite-volume numerical schemes to simulate shocks also provides implicit SGS models suitable for turbulent flow.

Modified equation analysis provides an analysis framework to reverse-engineer desirable physics into the design of the numerical schemes for ILES. Modified equation analysis was used in the early formal comparisons (Fureby and Grinstein, 1999; Grinstein and Fureby, 2007) between MILES and traditional LES to show that a class of nonoscillatory finite-volume algorithms with dissipative leading order terms provides appropriate built-in (implicit) SGS models of a mixed tensorial (generalized) eddy-viscosity type. Modified equation analysis can examine specific implementation aspects of the numerical schemes, such as the effects of temporal integration schemes, and can address how prescribed anisotropies introduced by nonuniform adaptive gridding contribute to the implicit SGS stress tensor in the modified equations. Because implicit SGS model contributions associated with finite-volume discretizations can be formally cast in divergence form as their explicit counterparts in the modified equation analysis – equations (1.5) and (1.6), and volume integrals in the finite-volume representation naturally link with the discrete spatial filtering operation in LES – top-hat filtering, *finite-volume discretizations are formally favored for ILES*. Finite volume discretizations have also been motivated based on derived characteristics of the associated implicit SGS models from modified equation analysis (Fureby and Grinstein, 1999; Grinstein and Fureby, 2007; Margolin and Rider, 2010; Grinstein et al., 2023) – versus classical SGS models.

Ensemble Averaged Flow

Analysis of ensemble-averaged flow equations – carried out as that of the spatially filtered equations at the top of this section – would formally yield RANS modified equations analogous to those for LES, with substituted ensemble-averaging and spatial-filtering operations on the flow variables and substituted RANS and LES (explicit and implicit) SGS stresses and commutation terms. This CG similarity reflects the fact that (spectral) effects of ensemble averaging and spatial filtering on the velocity solutions resemble each other in their nature. However, a key difference between the LES and RANS equations relates to their limiting behavior as the grid size $h \rightarrow 0$, when only the equations associated with a properly designed (realizable) LES will approach the high fidelity (DNS) limit – Sections 1.3.3 and 1.5.

Finite-Scale Navier–Stokes

Generalizing the spatial (cubical) averaging results of Margolin and Rider (2002) to three-dimensional tensor coordinates, adding temporal averaging and prescribing length scale \mathcal{L} and timescale \mathcal{T} , to $O(\mathcal{L}^4, \mathcal{T}^4)$ the instantaneous Finite-Scale Navier–Stokes equations by Ristorcelli (2016) describe the transport of a passive scalar and momentum by an incompressible fluid ($u_{j,j} = 0$),

$$\frac{\partial \bar{c}}{\partial t} + \frac{\partial (\bar{c} \bar{u}_j)}{\partial x_j} = \mathcal{D}_s \frac{\partial^2 \bar{c}}{\partial x_j \partial x_j} - \mathcal{L}^2 \frac{\partial}{\partial x_j} \left(\frac{\partial \bar{c}}{\partial x_k} \frac{\partial \bar{u}_j}{\partial x_k} \right) - \mathcal{T}^2 \frac{\partial}{\partial x_j} \left(\frac{\partial \bar{c}}{\partial t} \frac{\partial \bar{u}_j}{\partial t} \right), \quad (1.7)$$

$$\frac{\partial \bar{u}_i}{\partial t} + \frac{\partial (\bar{u}_i \bar{u}_j)}{\partial x_j} = -\frac{1}{\rho} \frac{\partial \bar{p}}{\partial x_i} - \mathcal{L}^2 \frac{\partial}{\partial x_j} \left(\frac{\partial \bar{u}_i}{\partial x_k} \frac{\partial \bar{u}_j}{\partial x_k} \right) - \mathcal{T}^2 \frac{\partial}{\partial x_j} \left(\frac{\partial \bar{u}_i}{\partial t} \frac{\partial \bar{u}_j}{\partial t} \right) + \nu \frac{\partial^2 \bar{u}_i}{\partial x_j \partial x_j}, \quad (1.8)$$

$$-\frac{1}{\rho} \nabla^2 \bar{p} = \frac{\partial \bar{u}_j}{\partial x_i} \frac{\partial \bar{u}_i}{\partial x_j} + \mathcal{L}^2 \frac{\partial \bar{u}_j}{\partial x_i \partial x_k} \frac{\partial \bar{u}_i}{\partial x_j \partial x_k} + \mathcal{T}^2 \frac{\partial \bar{u}_j}{\partial t \partial x_i} \frac{\partial \bar{u}_i}{\partial t \partial x_j}, \quad (1.9)$$

where the overbars indicate spatial and temporal averaging in a fixed Eulerian coordinate system over length scale \mathcal{L} and timescale \mathcal{T} .

The Finite-Scale Navier–Stokes framework reframes the computational questions of turbulence. In the continuum, the usual questions related to the velocity at a point and time, a concept limited computationally by finite volumes, mesh spacing h , and timestep Δt , and there are associated convergence issues as well as issues of consistent definition of finite-volume averaged velocities. The question Finite-Scale Navier–Stokes proposes to answer is different: What is the velocity in a finite volume (\mathcal{L}^3) over a finite time \mathcal{T} ? As the true and desired solution is an average over space and time (\mathcal{L} and \mathcal{T}), and the definition of averaged velocity will not change once $h < \mathcal{L}$ and $\Delta t < \mathcal{T}$, that is, there is no need for SGS modeling once the latter resolution limit can be achieved. Additional motivation for Finite-Scale Navier–Stokes approaches can be given in practical applications with inherently discrete (noncontinuum) requirements: for example, needed contaminant dispersal prediction for urban consequences management is dosages (contaminant in volume \mathcal{L}^3 over time \mathcal{T}).

The Finite-Scale Navier–Stokes solutions directly relate to laboratory observables, as measurement devices always involve finite space/timescales and cannot capture arbitrarily small-scales of high Re turbulence. By design, Finite-Scale Navier–Stokes models what is observable for a measurement device characterized by length and timescales \mathcal{L} and \mathcal{T} (e.g., thermocouple or hotwire width \mathcal{L} , instrumentation inertia \mathcal{T}).

Crucial insights follow from modified equation analysis studies for the Burgers (Margolin and Rider, 2002) and the NSE (Margolin, 2009) – demonstrating that leading order truncation (so-called) *errors* introduced by nonoscillatory finite-volume schemes represent physical flow regularization providing actual necessary modifications to the governing equations that arise when the motion of finite-scale observables is considered: *ILES works because it solves the equations that most accurately represent the dynamics of finite-volumes of fluid – governing the behavior of measurable physical quantities on the computational cells.*

SGS and SPG issues are typically intertwined and cannot be dealt with independently in many contexts of interest. This is the case – for example, when studying shock-driven turbulence generated via the RM instability (RMI, Brouillette 2002), where ILES has proven to be the effective CG simulation strategy because of its unique combination of shock and

turbulence emulation capabilities (Cohen et al., 2002; Leinov et al., 2009; Thornber et al., 2010; Grinstein et al., 2011; Gowardhan et al., 2011; Gowardhan and Grinstein, 2011; Haines et al., 2014). In what follows, we discuss CG characterization and requirements in terms of turbulence Reynolds number, revisit relevant realizability constraints for SGS modeling, and examine the impact of initial conditions on transition and predictions.

1.3.2 Turbulence Reynolds Number and the Mixing Transition

Transition to turbulence is traditionally viewed in terms of the rapid increase in the energy and the enstrophy production by mode coupling of a spectrum of smaller length scale motions. Transition can lead to an inertial range exhibiting Kolmogorov $-5/3$ wave-number power-law in the turbulence kinetic energy spectrum for sufficiently high Re (Dimotakis, 2000; Zhou, 2007) above the mixing transition threshold, $Re \sim 1 - 2 \times 10^4$ based on the integral length scale L (or $Re \sim 1 - 1.4 \times 10^2$ based on the Taylor microscale) (Dimotakis, 2000). A higher threshold, $Re \sim 1.6 \times 10^5$, is needed to achieve a minimum turbulent state (Zhou, 2007) – proposed as having enough large-/small-scale separation to ensure the robustness of macroscopic flow characteristics.

Transition is inherently dependent on initial conditions (George and Davidson, 2004b; Ristorcelli et al., 2013; Grinstein, 2017). Cascade pathways driven by vortex instabilities, self-induced deformations, stretching, and reconnections (Hussain and Husain, 1989; Grinstein, 1995, 2001; Leweke et al., 2016; Yao and Hussain, 2022) are fundamental building blocks to be captured by CG simulations.

The dimensionless ratio $D = \epsilon L/u^3 = (\epsilon/u^2)/(u/L)$ – ratio of dissipation to convection times, where u and L denote characteristic velocity fluctuation magnitude and length scale, has been extensively investigated as function of Re (Sreenivasan, 1984, 1998; Kaneda et al., 2003). Analysis of a large body of laboratory and simulation data suggests that a nondimensional parameter such as D approaches constancy when Re becomes sufficiently large. The data compiled by Sreenivasan (1984) exhibits consistent establishment of an inertial range and attaining asymptotic constant behavior $D \sim 1/2$ for Taylor-microscale based Re , $Re_\lambda > 50$. Further data analysis (Sreenivasan, 1998; Kaneda et al., 2003) suggests that somewhat higher Re_λ may be needed to achieve constancy of D , perhaps as high as $Re_\lambda \sim 200$, for which the inertial range is about one decade. The high- Re asymptotic results depict the noted viscosity-independent energy-dissipation-limit law for high *but finite* Re (Sreenivasan, 1984; Frisch, 1995) and are the basis for the fundamental turbulence scaling relation $\epsilon \sim u^3/L$.

Cascade mechanisms for high Re are believed to be mainly driven by Re -independent equilibrium dissipation. However, there is also reported evidence for significant high- Re nonequilibrium dissipation regimes existing in various turbulent flows in which the energy spectrum has Kolmogorov $-5/3$ wave-number scaling over a wide wave-number range, and for which distinctly different scaling relations supporting asymptotically nonconstant D apply (Vassilicos, 2015b) – see Chapter 11.

From an applied perspective, we can estimate a relevant CG effective Re (and hence an effective viscosity) for the simulated turbulence to assess the impact of resolution on predicted flow quantities and to characterize their macroscopic convergence. The ILES

effective kinematic viscosity can be defined as

$$\nu_e \equiv \nu + \nu_n, \quad (1.10)$$

where ν and ν_n are the molecular and numerical kinematic viscosities. The first component is a fluid property, whereas the second stems from the numerics and it is used by ILES as the SGS closure (Boris et al., 1992; Grinstein et al., 2010).

An expression for the numerical ILES kinematic viscosity ν_n in physical space can be obtained on dimensional grounds – based on local dissipation ε in a viscous fluid (Fureby and Grinstein, 1999; Wachtor et al., 2013),

$$\nu_n = \frac{\varepsilon}{2\langle S_{ij}S_{ij} \rangle}, \quad (1.11)$$

where $\langle \rangle$ denotes volumetric average, sum over repeated Roman indices is assumed, and S_{ij} is the strain tensor which can be readily evaluated based on the computed raw velocity data.

The dissipation ε can be determined by the prescribed momentum forcing for the homogeneous isotropic turbulence case, or related directly to the kinetic energy dissipation for unsteady turbulence. In the high- Re limit we can presume $D \approx 1/2$ (Zhou et al., 2014), and use

$$\varepsilon \sim Du^3/L. \quad (1.12)$$

With sufficiently resolved ILES having large-enough turbulence Re (scale separation) the cutoff lies within a simulated inertial range (e.g., Figure 1.15).

Evaluation of the ILES ν_n through equation (1.11) – based on the computed ratio of dissipation to squared strain-rate – characterizes the *turbulence dissipation in the inertial subrange of the simulated high- Re dominated flow*. It is distinct from the residual local “Newtonian fluid” numerical viscosity associated with the algorithm specifics through modified equation analysis directly affecting the smallest scales – characterizing the *simulated viscous dissipation* subrange.

Once a numerical viscosity ν_n is evaluated, an (effective) turbulence (Taylor microscale based) Re , can be computed as $Re_\lambda = u\lambda/\nu_e$, where u is the rms value of the velocity fluctuations, and λ is the Taylor microscale of the velocity fluctuations characterizing the inertial-range cutoff – Figure 1.15 – directly computable also in terms of suitably averaged measures of the raw velocity data,

$$\lambda = \left[\sum_{i=1}^{i=3} \sqrt{\langle u_i^2 \rangle / \langle u_{i,i}^2 \rangle} \right] / 3. \quad (1.13)$$

Wachtor et al. (2013) used established turbulence metrics and DNS data (Jiménez et al., 1993) to show that a well-designed ILES can accurately capture the mixing transition and asymptotic high- Re self-similar behavior (Figure 1.2), in terms of this effective turbulence Re .

1.3.3 Realizability Constraints for Subgrid-Scale Modeling

Mixing of a passive scalar θ by a fluctuating flow field is a classical problem in turbulence and relevant in many industrial flow applications. Overholt and Pope (1996) conducted

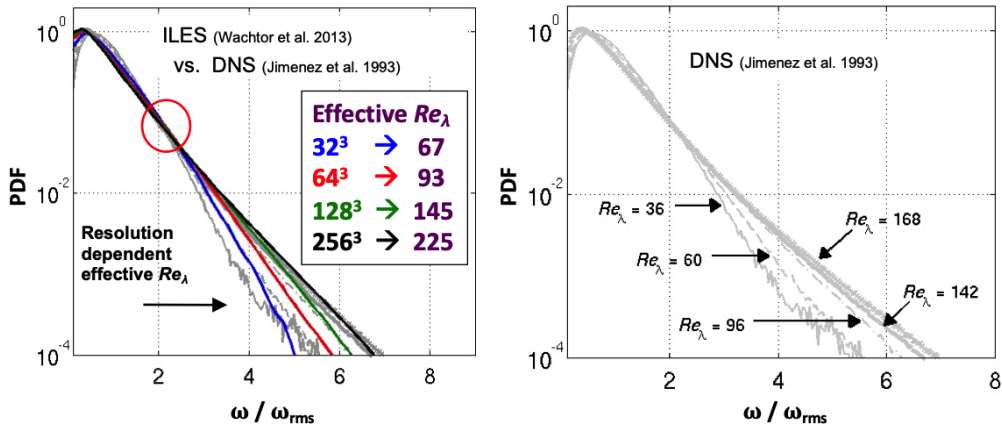


Figure 1.2 PDF of vorticity magnitude vs. Re_λ for homogeneous isotropic turbulence. Reprinted from Wachtor et al. (2013) with the permission of AIP Publishing.

DNS of $Sc \sim 1$ mixing of a passive scalar in the presence of a mean scalar gradient by forced, spatially periodic, isotropic turbulence. In this flow, a statistically steady-state scalar variance is achieved by balancing scalar variance production and dissipation. The passive-scalar mixing problem was first investigated with LES by Pullin (2000), who predicted that the normalized scalar variance asymptotically approaches a constant value as a function of Re – Figure 1.3a. Uncertain nonconstancy of the highest- Re DNS predictions (Gotoh and Watanabe, 2012) are clearly apparent due to fairly different sampling times ranging between 27 and 2.3 eddy-turnover times for Re between 174 and 586. Lower scalar variance predictions with ILES in Figure 1.3a are attributed to differences in the forcing schemes – and somewhat less to compressibility effects since the solenoidal velocity component is responsible for the generation of a passive scalar flux and subsequent scalar stirring (Blaisdell et al., 1994).

A scalar Taylor micro-scale, λ_θ , can be defined in terms of the raw scalar simulation data as its velocity analog λ – equation (1.13). The squared ratio of Taylor microscales, proportional to the velocity-to-scalar dissipation time ratio \mathcal{R} , was also reported to be asymptotically constant as function of Re by Pullin (2000), albeit comparisons with the early DNS (Overholt and Pope, 1996; Yeung et al., 2002) were inconclusive – Figure 1.3b. Analysis of subsequent results from DNS (Gotoh and Watanabe, 2012) and theory (Ristorcelli, 2006) shows the continued growth of \mathcal{R} consistent with high- Re nonequilibrium dissipation variability (Vassilicos, 2015b).

Figure 1.3b also shows that the \mathcal{R} results by Pullin (2000) rapidly decrease with Re when the explicit scalar SGS model is turned off – whereas ILES also without an explicit scalar SGS term (Wachtor et al., 2013) – exhibits neither decreasing nor asymptotically constant behavior but shows continued growth over the simulated range of effective Re consistent with the available high Re data. Associated with equilibrium dissipation *actually built* into the LES modeling (Misra and Pullin, 1997), Re -independence of \mathcal{R} for high Re is predicted

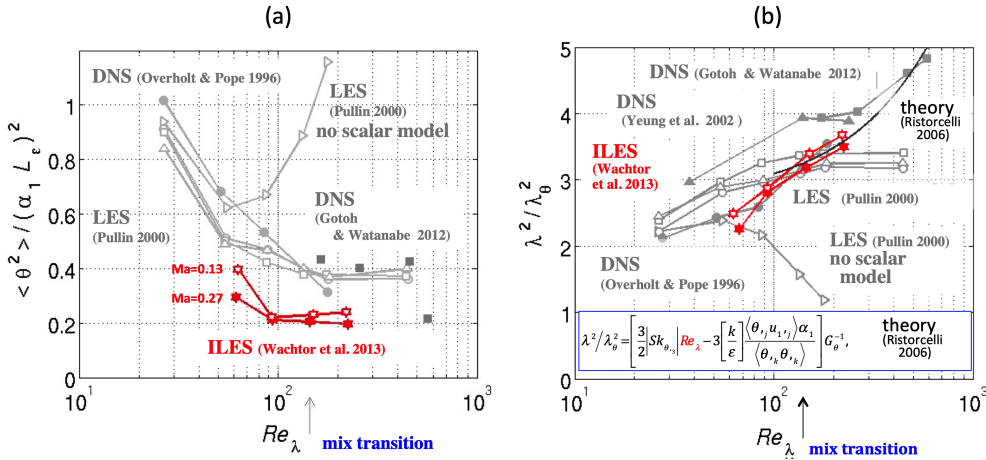


Figure 1.3 Predictions vs. Re . (a) Scalar variance. (b) Velocity-to-scalar dissipation time ratio. Reprinted from Wachtor et al. (2013) with the permission of AIP Publishing.

by Pullin’s LES. On the other hand, equilibrium dissipation *not built* into DNS, theory, and ILES allows variability of \mathcal{R} as a function of Re for high- Re .

Availability of more accurate high- Re reference data would be clearly helpful to elucidate these issues. However, on a more basic note, the fact that desirable modeling features can appear naturally built into a numerically well-designed ILES – but not necessarily in a mainstream classical LES strategy – reiterates a crucially required CG constraint: *realizable CG predictions must approach their well-established high fidelity counterparts as grid resolution is refined.*

1.3.4 Initial Conditions Modeling

Impact on Transition

Prescribing appropriate initial conditions is critical to emulate transition to turbulence (Druault et al., 2004; Verfaillie et al., 2006; Patnaik et al., 2007; Gowardhan and Grinstein, 2011; Grinstein et al., 2011). Use of single-point data is insufficient to characterize initial conditions and *white noise* fluctuations are inadequate because they quickly relaminarize. Initial conditions having *red noise* fluctuation content involving characteristic finite wavelength information on coherent structure turbulence (e.g., space and time correlations) are required. Effective initialization strategies have been proposed and demonstrated (Druault et al., 2004; Verfaillie et al., 2006).

Transition has been examined in the CG simulation context for the Taylor–Green vortex (TGV). TGV is a well-defined flow initialized with 3D solenoidal initial conditions, used as a prototype for vortex stretching, instability, and production of small-scale eddies to examine the dynamics of transition to turbulence based on DNS (Brachet et al., 1983; Frisch, 1995). The TVG case has also been used to demonstrate how convective numerical diffusion effects of certain algorithms can be effectively used by themselves to emulate the

dominant SGS physics of transition to turbulence for high (but-finite) Re flows (Drikakis et al., 2007; Grinstein et al., 2011). The TGV transition involves successive vortex self-inductions, stretching, and reconnections of counterrotating vortex pairs (Grinstein, 1995, 2001). The TGV involves triple-periodic boundary conditions enforced on a cubical domain and a uniformly spaced computational grid. The flow is initialized with prescribed 2D or 3D solenoidal velocity field conditions, and the pressure is a solution of the Poisson equation for the given velocity field. An ideal gas equation of state for air and incompressible (Brachet et al., 1983) or low-subsonic conditions have been considered (Drikakis et al., 2007; Grinstein et al., 2011).

Grinstein (2017) exploited the simplicity of the TGV test case to inquire regarding the effects of initial conditions dimensionality on transition to turbulence. Figure 1.4 shows visualizations illustrating the evolution of the two TGV cases, both run under similar conditions with ILES based on using the directionally split xRAGE code (Gittings et al., 2008; Grinstein et al., 2011) on the same uniform 256^3 grid. Figure 1.4b shows that there is transition and significant enstrophy growth when 3D initial conditions and 3D flow physics are involved in the simulations. By contrast, by imposing 2D initial conditions (Figure 1.4a), the numerically induced white noise is insufficient to trigger vortex-dynamics-based cascade mechanisms promoting the growth of 3D modes: The flow remains 2D – despite 3D convection being allowed, with enstrophy remaining largely unchanged. These results demonstrate that initial conditions' dimensionality matters to transition to turbulence. We also noted such absence of transition – in terms of insufficient enstrophy and turbulent kinetic energy production, in 3D simulations of laser-driven turbulent mixing starting from 2D initial conditions (Haines et al., 2014).

Initial Material Interface Conditions: Bipolar Richtmyer–Meshkov

Accurate and reliable simulation of material interfaces is essential to simulating material mixing dynamics. Material interfaces can be miscible or immiscible, with the character changing during the evolution of a system. This causes numerical approximations to the flow physics to be extremely challenging because the basic features of the approximations need to be dynamic, that is, adapt to the evolution of the materials. For example, in applications of interest such as inertial confinement fusion capsule implosions, an interface may begin as sharp and immiscible (solid/gas) and then evolve into a state where it mixes at an atomic level with neighboring material due to the effects of temperature and diffusion, or as it becomes a plasma.

Detailed material interface characteristics are initial conditions for the flow instabilities, and among the most crucial issues associated with these details is the sensitivity of late-time consequences to initial conditions specifics: Small variations in the initial state of the interface can result in quite significant changes to even the integral character of a mixing layer at late-times (George, 1989; Grinstein et al., 2011).

Initial material interface morphology controls the evolution of the RMI; distinctly different growth rate trends and material mixing consequences result depending on whether first-shocked relatively flat thin material interfaces or reshocked interfaces highly corrugated and nonlinear from the outset are involved; this so-called bipolar behavior of RMI presents significant challenges for moment closure modeling, and for its verification, validation, and uncertainty quantification metrics (Ristorcelli et al., 2013). Miscible gas–material interface

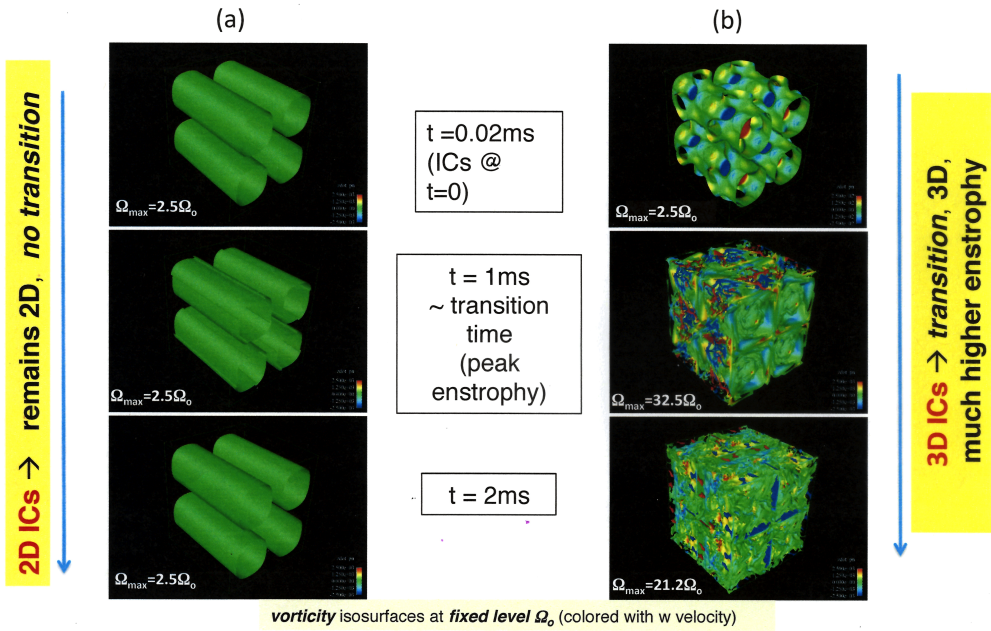


Figure 1.4 Taylor–Green Vortex starting from 2D (a) and 3D (b) initial conditions. Reprinted from Grinstein (2017), with permission from Elsevier; see the paper for details.

modeling strategies have used various superpositions of perturbation modes (Grinstein, 2016) in the simulation of shock-driven turbulence.

The initial interfacial morphology can be statistically characterized by the initial root-mean-square (*rms*) slope, $\eta_o = \kappa_o \delta_o \sim [\nabla\chi\nabla\chi]^{1/2}$, where χ is the local deviation of the initial material interface around the mean interface location, $\kappa_o = 2\pi / \lambda_o$, λ_o is a representative wavelength of the multiscale perturbation in the initial interface and $\delta_o = \delta(t = 0)$ denotes the initial interface thickness (Figure 1.5). High value of η_o denotes highly corrugated interfaces with high *rms* slope (Figure 1.6).

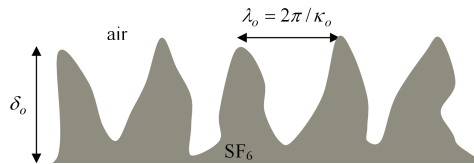


Figure 1.5 Schematic of interface morphology characterization. Reprinted from Gowardhan et al. (2011), with the permission of AIP Publishing.

Following Richtmyer (1960), the passage of a shock through the material interface has the effect of having deposited baroclinic vorticity growing as $\sim \eta_o$. For low η_o , less baroclinic vorticity is generated. When the initial characteristic wavelength is greater than its characteristic amplitude, crests and troughs are well separated, and vortices are weaker and

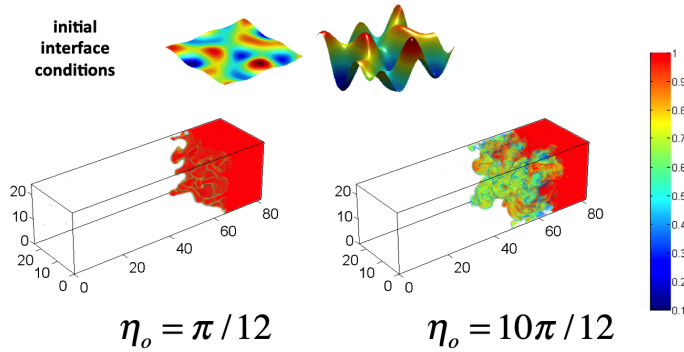


Figure 1.6 The bipolar RM behavior (Gowardhan et al., 2011; Ristorcelli et al., 2013); initial interface conditions are depicted on the top and instantaneous mix visualizations 3,000 μs are shown below. Reprinted from Gowardhan et al. (2011), with the permission of AIP Publishing.

consequently do not interact strongly. In this low η_o regime, the modes mainly grow in the shock direction in a ballistic (noninteracting) fashion. For high η_o , more baroclinic vorticity is generated. The initial characteristic wavelength is less than its characteristic amplitude, thus, crests and troughs of the perturbations are closer together, and the vortices are stronger and create new modes through nonlinear processes. For these flows, there is rapid production of smaller scales consistent with a transition to turbulence. The borderline case is $\eta_o \approx \pi$.

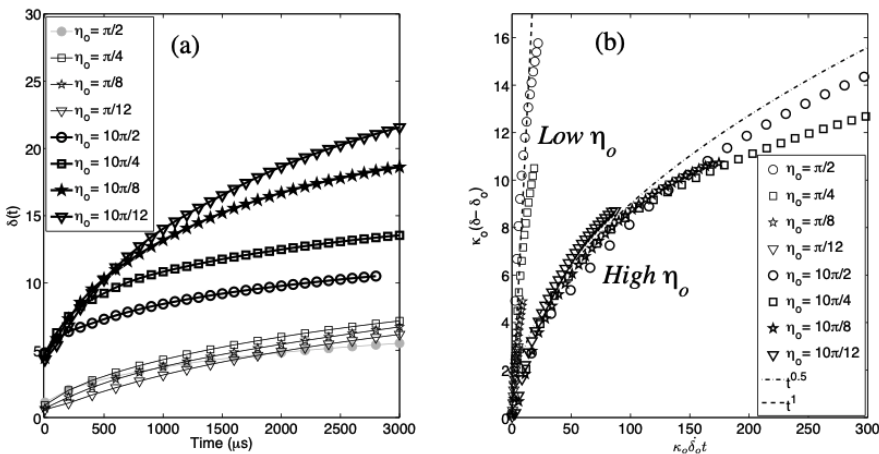


Figure 1.7 The bipolar RM behavior (Gowardhan et al., 2011). Evolving mix widths vs. time plotted in dimensional (a) and nondimensional form (b). Reprinted from Gowardhan et al. (2011), with the permission of AIP Publishing.

Distinctly different instability behaviors arise depending on initial *rms* interface slope η_o – linear RMI for low η_o and nonlinear RMI for high η_o . Despite the similarity in problem geometry, linear and nonlinear RMI share no dynamical or statistical features. We recognize

the nonlinear RMI as occurring when a high- η_o interface is first-shocked (Gowardhan et al., 2011) and in the reshock situations (Ristorcelli et al., 2013). Both latter configurations involve high initial *rms*-slope η_o , both exhibit the same scalings and collapse of data and are also very different from the low- η_o (linear) RMI. A simple way to demonstrate the very large physical differences between linear and nonlinear RMI is with the first-shocked problem, shown in Figure 1.7 from Gowardhan et al. (2011) and its trends with η_o . Instantaneous visualizations of at the selected time, $t = 3,000 \mu\text{s}$ shown in Figure 1.6 suggest material (interpenetration) mixing increasing with η_o .

1.3.5 Late-Time Predictions

The shock-accelerated material interface with a high initial *rms* slope is (by far) the most challenging known example of acute sensitivity to initial conditions. This is due to the large amplification a shock has on the various parameters of the initial interface and the fact that the problem actually comprises a group of instabilities – beyond just the linear RMI. Extreme sensitivity to material interfacial conditions at reshock time (Gowardhan et al., 2011; Gowardhan and Grinstein, 2011; Ristorcelli et al., 2013) raises late-time predictability issues.

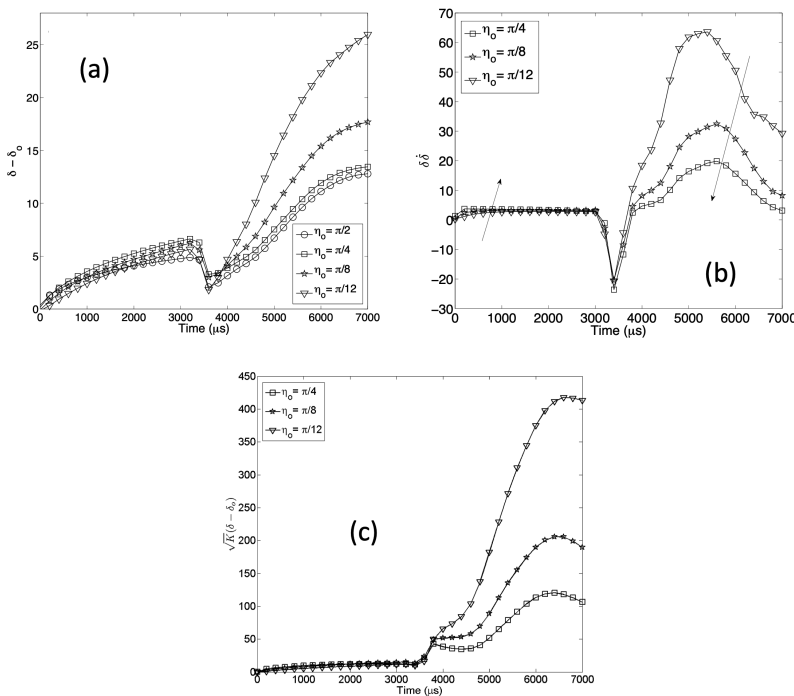


Figure 1.8 Mix width thickness (a), bulk Re (b) and turbulent eddy viscosity (c) for shocked/reshocked planar shock tube ILES (reshocked at $t = 3,700 \mu\text{s}$) as a function of initial *rms* slope η_o – see Ristorcelli et al. (2013). Arrows indicate the direction of increasing initial *rms* slope η_o , and K denotes turbulent kinetic energy. Reproduced from Ristorcelli (2016).

The impossibility of very long-range weather forecasting (Lorenz, 1963), appropriately comes to mind here. Because of chaotic variability associated with unavoidable small perturbations (uncertainties) of presumed SGS and SPG conditions, it may become impossible – even within a mathematically well-posed dissipative flow simulation framework – to provide realistic late-time solutions to address questions of interest (e.g., very-long-range weather forecasting).

Figure 1.8 from Ristorcelli et al. (2013) shows the results of shocking a planar interface twice: first-shocked at $t = 0$, at which time initial *rms* slope is in the linear RMI regime, and reshocked at $t = 3,700$ ms, at which time the material interface has high initial *rms* slope. We plotted as functions of time, mix-layer width, bulk Re , and turbulent eddy-viscosity – used to scale nonlinear-to-linear interactions of the flow. After reshock, mixed layer response and growth trends are hugely different. *The various cases in Figure 1.8 have similar values of layer thickness and eddy viscosity at reshock time – followed by rapid divergence of metrics trajectories*, indicating that simple initial conditions characterization in terms of mix width and kinetic energy – typical with engineering turbulence models, is insufficient.

The predictability problem manifests itself as a rapid divergence of the trajectories and depends on subtleties of the balance of various possible instability mechanisms (beyond linear RMI) during enstrophy deposition and generation in high *rms*-slope interfaces in ways that are unknown. Such sensitivity to initial conditions at reshock is also observed in other configurations (Gowardhan and Grinstein, 2011; Balasubramanian et al., 2012) and raises serious questions regarding repeatability of numerical and laboratory experiments and requirements to achieve predictability for the problem at hand: *What are appropriate reduced models for the initial conditions? What are appropriate ensemble averages of solutions covering the relevant initial condition variability? What are usefully complete set of convergence metrics?*

1.4 Coarse-Graining Shocked Gas Curtain Turbulence

Shocked gas curtain (GC) experiments at LANL were designed to validate simulation model capabilities (Balakumar et al., 2008; Orlicz et al., 2009). The SF₆ GC (Figure 1.9) is formed by forcing SF₆ through a linear arrangement of round nozzles into the shock-tube test section; the GC is stabilized using co-flowing air and suction at the bottom of the curtain (Balakumar et al., 2008). The developed GC is shocked ($Ma = 1.2$), and its later evolution subject to RMI, transition, and nonequilibrium turbulence phenomena is investigated. Analysis in the laboratory experiments is based on particle image velocimetry and planar laser-induced fluorescence data acquired at the selected horizontal plane, 2 cm below the beginning of the GC (Figure 1.9). Typically, available data involves intensities (relative SF₆ concentration) at the plane of measurement. The GC can be reshocked at times controlled by the location of a reflecting wall to examine the effects of initial conditions at reshock time on turbulence development and mixing.

Our strategy was to produce a well-defined starting GC with realistic 3D initial conditions characteristics for the LES studies. We carried out separate GC simulations to emulate the physics of a mixture of SF₆ and air falling through the shock-tube test section constrained by the available laboratory GC information (Gowardhan and Grinstein, 2011). Various ways of superimposing synthetic noise to the baseline varicose (nonperturbed) simulated GC were also additionally tested. Configurations with carefully controlled initial conditions were

considered, differing from each other on the specifics of modeled low-amplitude multimode fluctuations. This was achieved: (a) by slightly offsetting the nozzles in the shock (x_1) direction and (b) by adding 3D perturbations to the initial (simulated) GC concentration field.

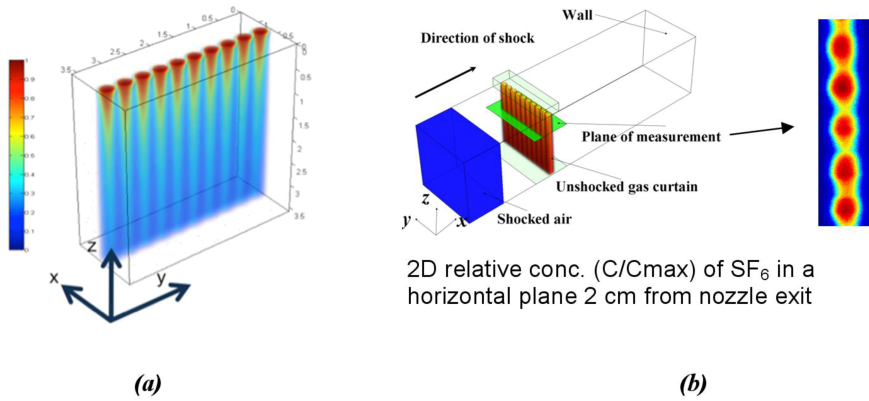


Figure 1.9 (a) Steady-state GC in terms of SF_6 volume of fraction distributions, (b) schematic of experiments. From Gowardhan and Grinstein (2011), reprinted by permission of the publisher.

1.4.1 Hydrodynamics Modeling and Mach Number Effects

To investigate the impact of the numerical scheme on the GC predictions, Pereira et al. (2020) conducted a series of studies based on three distinct numerical approaches: (i) the HLL (Harten et al., 1983) Riemann solver applying Strang splitting and a Lagrange-plus-Remap formalism (Colella, 1982; van Leer, 1997) to solve the directional sweep (see Gittings et al. (2008) for details); (ii) the HLLC (Toro et al., 1994) Riemann solver using a directionally unsplit strategy and parabolic reconstruction (Colella and Woodward, 1984); and (iii) the HLLC (Toro et al., 1994) Riemann solver using a directionally unsplit strategy, parabolic reconstruction (Colella and Woodward, 1984), and added low-Mach correction (LMC, Thornber et al. 2008) *explicit* SGS model. The numerical schemes are denoted split, unsplit, and unsplit*, respectively.

Directionally unsplit algorithms are needed when distortions introduced by split schemes are unacceptable: for incompressible or nearly incompressible flows and magnetohydrodynamic systems – where solenoidal conditions must be captured, and for flows involving a high degree of initial symmetry as with inertial confinement fusion capsule implosions – Chapter 16.

By incorporating the LMC SGS model, we additionally address the problem of leading numerical dissipation $\sim Ma^{-1}$ associated with upwinding in shock-capturing schemes at low Ma – Section 1.4.3. LMC unsplit hydrodynamics accurately captures the physical effects of vortex stretching and other basic flow instabilities driving mixing in the low- Ma regimes where most mixing of interest occurs, resulting in further improved accuracy relative to the default (split) hydrodynamics for significant computational cost savings (Grinstein et al.,

Table 1.1 Numerical Hydrodynamics Details.

	Solver	Splitting operator	Remap	LMC	
Split	HLL	Split	Lagrange	No	ILES
Unsplit	HLLC	Unsplit	Direct Eulerian	No	ILES
Unsplit*	HLLC	Unsplit	Direct Eulerian	Yes	LES

2019, 2023). The main characteristics of these schemes are summarized in Table 1.1, and their comprehensive description is given by Gittings et al. (2008) and Grinstein et al. (2019). The main results of this study are summarized in what follows – see Gowardhan and Grinstein (2011) and Pereira et al. (2020) for more details.

The GC evolution predicted by the three numerical schemes is plotted in Figure 1.10. The results are compared against the experiments of Balakumar et al. (2008). In Figure 1.10, the GC is defined by the concentration intensity of SF₆, $I_{SF_6} = (c_{SF_6}) / (c_{SF_6})_{max}$, measured at the plane $x_3 = 20$ mm. Figure 1.10 indicates that the results of the three numerical schemes are in good agreement before reshock, and show small discrepancies against the experimental observations. At $t = 0$, the varicose GC is at rest, and the shock wave is about to strike it. For later times, the shock-wave passes through the GC, leading to its compression and deposition of vorticity at the fluids’ interface by baroclinic mechanisms ($t = 20 \mu s$). This triggers the mixing of the two fluids. The numerical predictions exhibit a strong dependence on the numerical scheme, which affects their agreement with the experiments. Compared to the unsplit schemes, the split scheme predicts a thinner mixing layer than that reported experimentally, which is featured by a heterogeneous mixture where it is possible to observe lumps of fluid. In clear contrast, the simulations based on the more accurate unsplit schemes agree significantly better with the laboratory experiments. Only the unsplit* scheme can predict the cloud-like, depicting the small-scale mixing features observed in the experiments.

The three numerical schemes lead to fairly similar values of Ma for the simulated time (Pereira et al., 2020). Whereas Ma does not exceed 0.40 before reshock, it remains under 0.10 after reshock and can even reach 0.04 at $t > 820 \mu s$ (Pereira et al., 2020). This is a reduction of one order of magnitude to values of Ma typical of incompressible flow. Given, as noted, that local numerical diffusion in simulations using upwinding schemes typically scales with Ma^{-1} (Book et al., 1991; Guillard and Murrone, 2004; Thornber et al., 2008), we attributed the local differences between late-time solutions to different local magnitude of Ma . At such times after reshock, $O(Ma) = 10^{-2}$ so that the characteristic numerical diffusion in the split and unsplit computations is thus expected to be significantly larger than that for unsplit*. This highlights the crucial role of the LMC (Thornber et al., 2008) in improving the simulations’ quality.

1.4.2 Effective Reynolds Number (Re_e)

One of the main consequences of modeling a fraction of the turbulence spectrum is the reduction of the flow effective Reynolds number, Re_e ,

$$Re_e = \frac{uL}{\nu_e}. \tag{1.14}$$

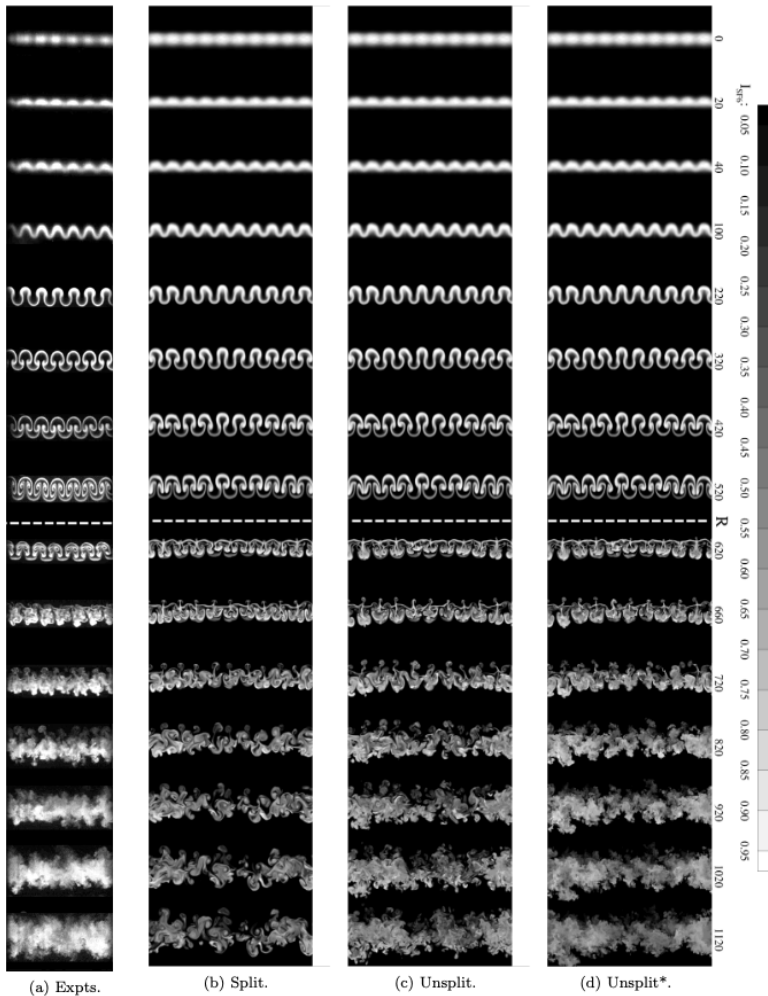


Figure 1.10 Evolution of the SF_6 intensity I_{SF_6} for distinct numerical schemes (Pereira et al., 2020) and experiments (Balakumar et al., 2008). Reprinted from Pereira et al. (2020), with permission from Elsevier.

This is driven by the increase of the flow effective viscosity, which is responsible for diminishing the computational requisites of the simulations. In equation (1.14), L is a reference length scale, u is the velocity scale, and ν_e is the flow effective viscosity, which entails the molecular ν (fluid), numerical ν_n (numerical truncation), and turbulent ν_t (closure) kinematic viscosities.

Although such modeling strategies are of importance to the simulation of practical flow configurations, an excessive reduction of Re_e may preclude the precise prediction of the selected problem by suppressing fundamental flow processes such as instabilities and coherent structures. Pereira et al. (2018, 2019) demonstrated the relevance of this aspect by identifying

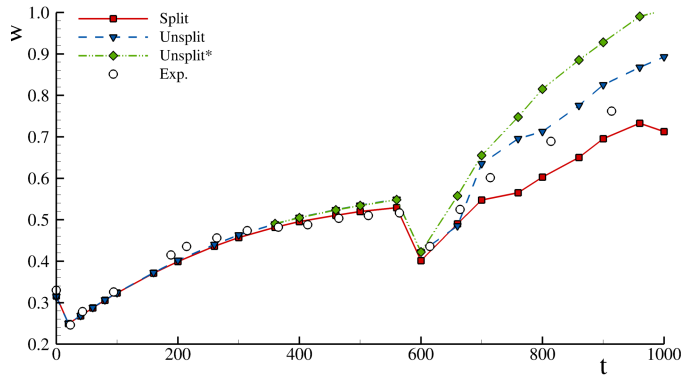


Figure 1.11 Evolution of the mixing-layer width w with various numerical schemes (Pereira et al., 2020); experiments from Balakumar et al. (2008). Reprinted from Pereira et al. (2020), with permission from Elsevier.

the coherent structures governing the flow dynamics around circular cylinders in subcritical regimes, and estimating the minimum Re_e (from experiments) to capture such phenomena.

As the present flow dynamics at late-times is governed by presumably turbulent mixing layers, we can now correlate the outcome of the three schemes with the magnitude of Re_e . To this end, the effective computational Reynolds number Re_e can be estimated as in Grinstein et al. (2019) – following Zhou et al. (2014),

$$Re_e = \frac{6w^2}{k} s_{ij}s_{ij}, \tag{1.15}$$

where w is a mixing width measure (Figure 1.11), k is the total kinetic energy defined as $k = \sum u_i^2/2$, and s_{ij} is the strain-rate tensor. We emphasize that k and s_{ij} consider the complete velocity field – mean, coherent, and turbulent (Hussain and Reynolds, 1970; Schiestel, 1987), so that the estimated Re_e represents an upper limit for its magnitude.

Figure 1.12 shows the temporal evolution of Re_e obtained with the three numerical schemes. Until reshock, the results indicate that Re_e is clearly inferior to the Dimotakis’ mixing transition Re (Dimotakis, 2000) – $Re_c = 1.0 \times 10^4$ and 2.0×10^4 . By contrast, the predictions of the three schemes show distinct tendencies after reshock. The results show that Re_e for split scheme calculations is always significantly lower than the critical Reynolds number Re_c . This is the reason why the mixing layer predicted by this scheme does not exhibit high-intensity turbulence flow features or a homogeneous mixture.

On the other hand, the simulation based on the unsplit scheme exceeds the lower limit of the Re_c band at $t > 800 \mu\text{s}$ but not its upper limit. In comparison to split, this explains the quality enhancement observed in unsplit predictions. Yet, the fact that Re_e is within the lower and upper limits of Re_c suggests that the observed low degree of heterogeneity is caused by the magnitude of Re_e . Finally, Figure 1.12 indicates that only the unsplit* scheme can clearly exceed the Re_c after the reshock. For instance, it is observed that Re_e is almost two times larger than Re_c at $t = 800 \mu\text{s}$. The larger values of Re_e enable unsplit* computations to better simulate the turbulent mixing layer of the present flow.

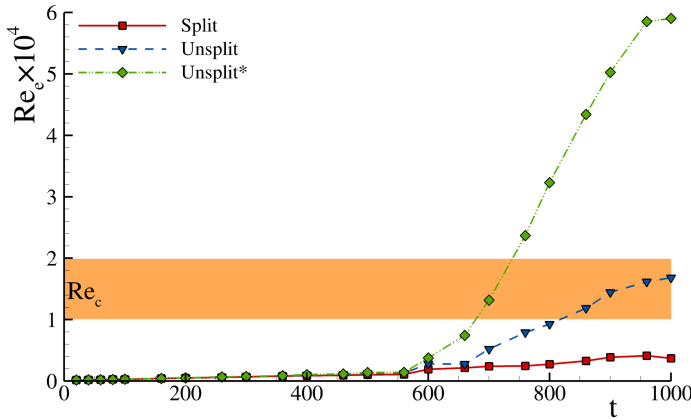


Figure 1.12 Temporal evolution of the effective Reynolds number, Re_e , for distinct numerical schemes. Reprinted from Pereira et al. (2020), with permission from Elsevier.

1.4.3 Vorticity Production Budget

Next, we investigate the effect of the numerical hydrodynamics scheme on the inviscid mechanisms contributing to the production of vorticity. This constitutes a crucial step in interpreting the results because the shock-driven mixing problem is triggered by baroclinic deposition of vorticity at the fluids' interface and depends on the vorticity dynamics. The evolution of the dominant inviscid mechanisms responsible for vorticity production, ω , in the mixing layer (shockwise direction) is depicted in Figure 1.13 (Pereira et al., 2020). Vorticity production mechanisms are stretching, S_i , dilatation, D_i and baroclinic, B_i ,

$$S_i = \omega_j \frac{\partial u_i}{\partial x_j}, \quad (1.16)$$

$$D_i = \omega_i \frac{\partial u_j}{\partial x_j}, \quad (1.17)$$

$$B_i = e_{ijk} \frac{1}{\rho^2} \frac{\partial \rho}{\partial x_j} \frac{\partial p}{\partial x_k}, \quad (1.18)$$

so that,

$$\frac{\partial \omega_i}{\partial t} + u_j \frac{\partial \omega_i}{\partial x_j} \sim S_i - D_i + B_i, \quad (1.19)$$

where ω_i is the Cartesian component of the vorticity vector. The terms S_i and D_i are responsible for the production of vorticity by vortex stretching (Tennekes and Lumley, 1972; Davidson, 2006) due to velocity gradients and compressibility effects, and B_i represents baroclinic production of vorticity driven by the misalignment of the pressure and density gradients.

Figure 1.13 shows that production of vorticity in the mixing layer is governed by the baroclinic mechanism up to reshock time, for $t < 600 \mu\text{s}$. This behavior is observed for all numerical schemes and also for the other cartesian coordinates x_i . However, the influence

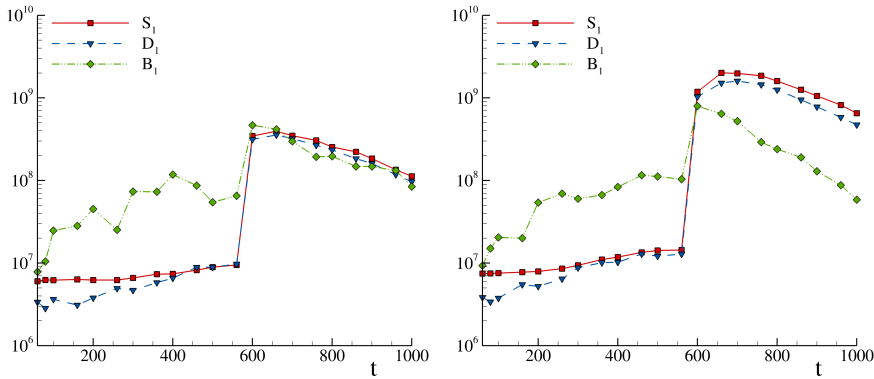


Figure 1.13 Temporal evolution of the x_1 component vorticity production terms (S_1 , D_1 , and B_1); left frame: split; right frame: unsplit*. Reprinted from Pereira et al. (2020), with permission from Elsevier.

of each production mechanism and numerical scheme in the vorticity dynamics changes after reshock ($t > 600 \mu\text{s}$), and vorticity production experiences a substantial increase after reshock. This tendency is independent of x_i (Pereira et al., 2020, 2021) and numerical scheme.

The most significant result in Figure 1.13 is the fact that the values of S_1 and D_1 can surpass those of B_1 by more than one order of magnitude. This occurs for the unsplit* scheme, it is independent of the Cartesian component (Pereira et al., 2020, 2021) and demonstrates that the production of vorticity at late-times is governed by stretching and dilatation mechanisms. This is typical of turbulent flow. Figure 1.13 also shows that the magnitude of the production mechanism depends on the numerical scheme.

Whereas split leads to similar values of the three vorticity production mechanisms, the unsplit schemes predict substantially larger contributions of S_1 and D_1 than B_1 . As we switch from split to unsplit*, the relative importance of S and D grows in relation to B . This explains the larger unsteadiness of unsplit* solutions since S and D are closely dependent on the turbulent field. Overall, the vorticity production budgets shown in Figure 1.13 reiterate the close relation between the numerical scheme and the quality of the predictions. The numerical hydrodynamics can alter fundamental mechanisms governing the flow dynamics.

1.4.4 Bipolar Richtmyer–Meshkov Behavior

Despite the significantly more complex GC shock-tube configuration having fairly different features (separate and diffused initial material interfaces in the GC versus single material interface in the planar shock tube), we found it possible to also demonstrate a similarly useful realization of the bipolar RM initial conditions parameterization and data reduction in terms of an appropriate characteristic single parameter (Gowardhan and Grinstein, 2011) – Figure 1.14.

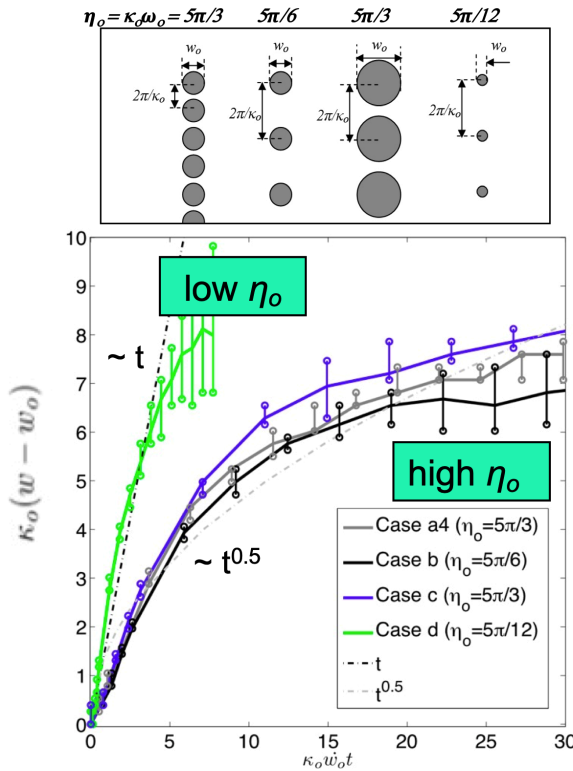


Figure 1.14 Bipolar Richtmyer–Meshkov for the double-interface GC shock tube from Gowardhan and Grinstein (2011). The *rms* slope parameter $\eta_o = \kappa_o w_o$ is defined in terms of the jets’ separation $2\pi/\kappa_o$ and jet diameter w_o . From Gowardhan and Grinstein (2011), reprinted by permission of the publisher.

1.5 Dynamic Coarse-Grained Turbulent Mixing

Strategies bridging LES and RANS are being actively pursued for aerospace and automobile full scale simulations (Frolich and von Terzi, 2008) – albeit RANS is still widely used. Blended hybrids such as the *flow simulation methodology* (FSM, Speziale 1998; Fasel and von Terzi 2006) scale closure terms on RANS equations by a contribution function $0 < f(\Delta/L) < 1$, where Δ is the local grid size and L is a reference bridging length. The balance between modeled and computed dissipation is based on the RANS stress model R_{ij}^m locally morphing into SGS Favre-averaged LES stress SGS model \tilde{R}_{ij}^s ,

$$\tilde{R}_{ij}^s \equiv f(\Delta/L) R_{ij}^m, \tag{1.20}$$

where the contribution function $f(\Delta/L)$ vanishes in the high fidelity limit ($\Delta \rightarrow 0$) and approaches unity at the low-resolution limit (pure RANS). Formal relations such as (1.20) – involving ensemble-averaged RANS and spatially filtered LES quantities are interpreted in a generalized-function (integral) sense. Hybrids exploit the structural similarity of equations for

RANS and LES and use relationships between filtering and averaging operations (Germano, 1992).

Flow simulation methodology was originally intended to locally bridge DNS and RANS as a function of grid resolution. More generally, FSM can be used to locally blend a high-fidelity simulation strategy with RANS to generate a sophisticated LES strategy in between. The issue of interest is the computation of the dissipation, which must be supplemented by the model for underresolved flow conditions. For sufficiently fine resolution, the dissipation range is resolved, and the RANS contribution should switch itself off – that is, $f(\Delta/L) \rightarrow 0$ as $\Delta \rightarrow 0$. In the FSM approach first proposed by Speziale (1998) – and subsequently pursued in various forms by others, empirical *ad hoc* forms for the contribution function f were prescribed.

Dynamically solving for the contribution function based on decomposing the full stress into modeled and resolved components and using a differential filter as secondary filtering operation to define the resolved part was first proposed by Germano (1998) and recently extended by Grinstein et al. (2020, 2021) by additionally requiring the resolved stress to approach the full stress with grid resolution refinement to ensure realizability of the bridging-based LES. In our dynamic FSM paradigm for turbulent material mixing applications, the full stress is decomposed in terms of modeled \tilde{R}_{ij}^s and resolved T_{ij} parts,

We use LMC-xRAGE LES as a high-resolution limit strategy, there is no additional explicit SGS model to that provided by the LMC, and the hybrid \tilde{R}_{ij}^s is directly related to the RANS stress R_{ij}^m in terms of f through (1.20),

$$R_{ij}^{full} = \tilde{R}_{ij}^s + T_{ij}. \tag{1.21}$$

For consistency and realizability of the generated LES in approaching the high-resolution/fidelity limit, we require that $T_{ij} \rightarrow R_{ij}^{full}$ as $\Delta/L \rightarrow 0$. We enforce this additional modeling constraint, in terms of $\gamma = (\Delta/L)^l$, for $l \geq 1$, by assuming that R_{ij}^{full} can be approximated by a resolution-dependent weighted-average of the RANS and resolved stresses,

$$R_{ij}^{full} \sim \gamma R_{ij}^m + (1 - \gamma)T_{ij}. \tag{1.22}$$

We substitute equation (1.20) into (1.21), use equation (1.22), and after contracting with a generic tensor quantity q_{ij} – for example, $q_{ij} = T_{ij}$, we solve for f ,

$$f(\Delta/L) = \gamma\{1 - [q_{ij}T_{ij}]/[q_{ij}R_{ij}^m]\}. \tag{1.23}$$

By design, the contribution function enforces realizability of the bridging-based LES through (1.20) in the high fidelity limit $\Delta \rightarrow 0$, when LES \rightarrow DNS. The choice of l controls how the LMC LES SGS model is supplemented by the explicit SGS model generated by the bridging strategy for intermediate resolutions. For xRAGE numerics – first-order near shocks and second-order in smooth flow regions, $l \geq 2$ is a suitable choice.

Large eddy simulation is based on the newly available directionally unsplit LMC-xRAGE numerical hydrodynamics (Grinstein et al., 2019, 2020, 2021). The default second-order split xRAGE hydrodynamics (Gittings et al., 2008) was used in our earlier *sequential hybrid* ILES/RANS simulations of the shock-tube laboratory experiments (Grinstein, 2017) running pure ILES at early times to generate RANS initialization at selected prescribed start time. The present *blended* LES/RANS paradigm acts at all times, as well as the LES used as a reference. For consistency, we also require $f \equiv 1$ for $\gamma \geq 1$.

A detailed discussion of derivations and BHR initialization issues can be found in Grinstein et al. (2020, 2021). The Dynamic BHR formalism uses the Besnard–Harlow–Rauenzahn (BHR) multi-equation RANS framework (Besnard et al., 1992) in the BHR3.0 version (Schwarzkopf et al., 2011; Haines et al., 2013). Similar BHR extensions with the more recent BHR3.1 (Schwarzkopf et al., 2016) version are expected to be straightforward.

In the original FSM modeling bridging DNS and RANS (Speziale, 1998; Fasel and von Terzi, 2006), the bridging lengthscale L was an estimated Kolmogorov length scale. Choosing $L \sim$ Kolmogorov scale amounts to choosing L as the smallest hydrodynamic length scale in the turbulent flow, or, a small fraction of the Taylor microscale characterizing the smallest vortices of the turbulence. Likewise, for bridging LES and RANS, a computed Taylor microscale of the velocity fluctuations (λ_c) characterizing the CG simulations cutoff and simulated turbulence can be usefully considered (see Figure 1.15). Such computed Taylor microscale λ_c can be directly evaluated in terms of suitable volumetric-averaged functions of the raw velocity data $\{u_i\}$ (Wachtor et al., 2013) – equation 1.13. As λ_c is typically found to be ≥ 10 cells for LMC-xRAGE LES (Grinstein, 2020), choices of $L \sim$ few cells in what follows, amount to choosing L as small fraction of λ_c .

1.5.1 Planar Shock Tube

We revisit the planar shock-tube laboratory experiments by Poggi et al. (1998), involving high (SF_6) and low (air) density gases, Atwood number, $At = 0.67$, presumed geometries of the membranes and the wire mesh initially separating the gases, and reshock off an end-wall.

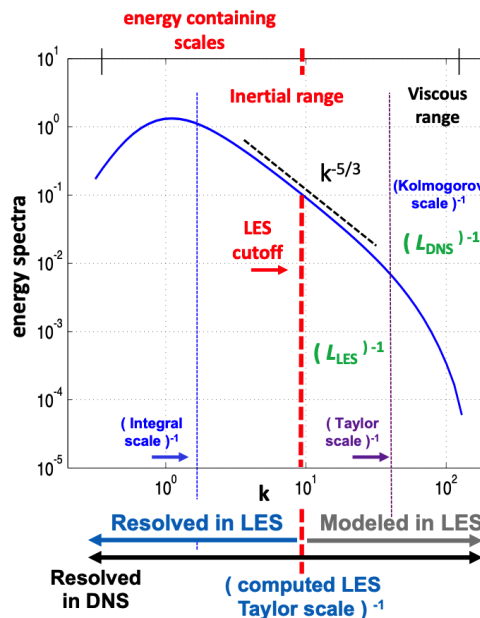


Figure 1.15 Bridging length L for RANS/DNS and RANS/LES hybrids. Reprinted from Grinstein (2020), with permission from Elsevier.

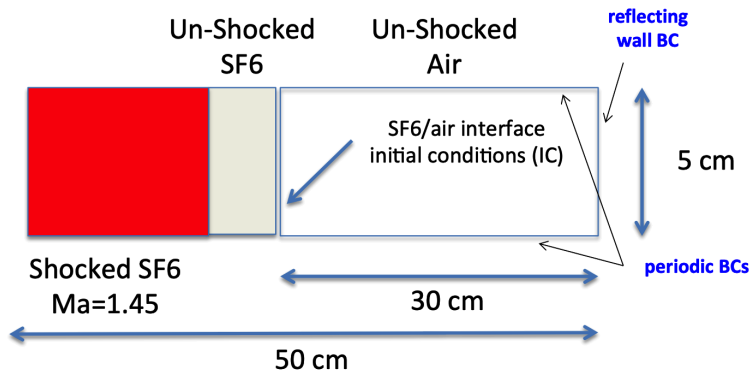


Figure 1.16 Schematic of the planar shock tube configuration.

A shocked SF_6 region is created upstream in terms of a higher-density higher-pressure SF_6 region for a Mach 1.45 shock (strength 0.54). The planar primary shock propagates in the through unshocked SF_6 , and then through the SF_6 /Air contact discontinuity. The shock propagates through the contact discontinuity and reflects at the end of the simulation box, where purely reflecting boundary conditions are enforced (Figure 1.16).

Early (0.05 mm resolution) planar shock-tube simulations by Mugler and Gauthier (2000) were based on the 2D NSE. In the more recent *sequential* xRAGE-ILES/BHR-RANS hybrid simulation studies (Grinstein, 2017), xRAGE-ILES generated data was used to provide physics-based initial conditions to BHR-RANS just before first reshock and was also used as a reference for its assessment. By prescribing ILES-generated 3D initial conditions and allowing for 3D convection with just enough resolution in Grinstein (2017), the computed dissipation in 3D RANS (vs. 2D RANS) was found to effectively supplement the modeled dissipation following 1st reshock. However, 3D RANS cannot resolve the subsequent consequences of a new transitional flow event at second reshock (Grinstein, 2017). This limitation is typical of a standalone RANS and motivates our pursuit of *blended* LES/RANS capable of dynamically adapting the simulation model to local flow conditions for applications driven by multiple shocks.

Spectral content and standard deviation are prescribed for the initial material sharp-interface conditions (Grinstein, 2017), in terms of superposition of six equally weighed wavelengths in the neighborhood of characteristic initial *egg-crate* length and mix thickness, h , and red-noise $\sim k^{-2}$ deformations with standard deviation $0.04h$ – with shortest wavelength of at least four coarsest cells.

Mix width, as well as velocity magnitude and variance data from the experiments (Poggi et al., 1998; Mugler and Gauthier, 2000) are used for benchmarking the LMC-xRAGE LES predictions (Grinstein et al., 2021). In turn, the LES results can then be used as a detailed reference for dynamic bridging mixing predictions – all generated with the same domain, same resolutions, and same initial and boundary conditions.

Compared to the laboratory experiments (Poggi et al., 1998), the computational domain in the present simulations (Figure 1.16) had the same (30 cm) initial interface-to-wall distance. As runtime compromise – as in Grinstein (2017), we focused again on the center 5×5 cm

transverse portion of the laboratory channel window section with periodicity imposed in the transverse (y, z) directions – in contrast with 8×8 cm channel cross-section limited by no-slip wall boundaries in the laboratory experiments.

Late-time discrepancies between computational and laboratory studies can be again expected due to effectively different boundary conditions in transverse directions and unaccounted effects of near-wall momentum deficit in actual experiments (Mugler and Gauthier, 2000). Grinstein (2017) found such disagreements after first reshock, for times $\gtrsim 1.4$ ms.

The initial material interface thickness δ_o in the laboratory experiments is not reported in the original paper (Poggi et al., 1998) and was chosen in Mugler and Gauthier (2000) to be a fraction of the *egg crate* wavelength in the laboratory experiments ($h = 1$ mm). The convenient computational resolution choice here is to use a single length scale for initial conditions, with the same characteristic initial wavelength h also used to prescribe $\delta_o = h$.

1.5.2 Large Eddy Simulation Validated with Experiment

The present 3D simulations use between two and eight levels of adaptive mesh refinement (AMR) with the finest resolutions ranging between 0.2 mm and 0.05 mm, respectively; the (more practically motivated) 3D dynamic xRAGE-BHR bridging simulations below use 2–4 levels of AMR with 0.100–0.200 mm resolution. The simulations typically used ~ 0.1 Billion (0.2 mm resolution), ~ 0.5 B (0.1 mm resolution), and up to ~ 5.2 B (0.05 mm resolution) computational cells. We use the third-order LMC xRAGE numerical hydrodynamics (Grinstein et al., 2019, 2020) as main strategy – versus *split* second-order xRAGE used in Grinstein (2017).

Figure 1.17 illustrates SF_6 mass fraction distributions near first-shock time – reflecting on initial conditions characteristics and at later times, before the first reshock and after the second reshock. Figures 1.18 and 1.19 compare the axial velocity magnitude and variance evolution versus those in the reported experiments (Mugler and Gauthier, 2000). As in the experiments, Figure 1.18 shows a first velocity plateau near 130 m/s corresponding to air accelerated by the incident shock wave, followed by a brief drop at 0 m/s corresponding to air decelerated by the first reflected shock on the end wall, and then by a second perturbed plateau which includes the crossing of the turbulent mixture reflecting gradually on the density gradient in the turbulent mixing zone. The present mean axial-velocity results for the latter plateau agree well with the experiments up to approximately $t \sim 1.3$ ms and then agree with the theoretical mean velocity of 47 m/s computed in Poggi et al. (1998) based on the Rankine–Hugoniot relations for transversely unbound flow (not affected by wall boundary layers). Reported differences between laboratory measured mean velocity (59 m/s) and the said theoretical expectation (47 m/s) have been attributed to the wall boundary-layer reversal effects in the SF_6 at shock crossing (Mugler and Gauthier, 2000). As noted, the present simulations do not account for the wall boundary layer effects – and that consistently also underlies the discrepancies with experiments in Figure 1.19 for $t \gtrsim 1.4$ ms. In agreement with the laboratory experiments, the second velocity plateau ends with the arrival of the second reflected shock wave on the end wall. The presently reported computed axial-velocity results are fairly independent of grid resolution.

Laboratory axial velocity variance (R11) data with $\pm 15\%$ estimated uncertainty was reported at locations of 161, 169, and 178.5 mm (Poggi et al., 1998), covering a range where turbulent mixing zone passages occur between its interactions with first and second reshock

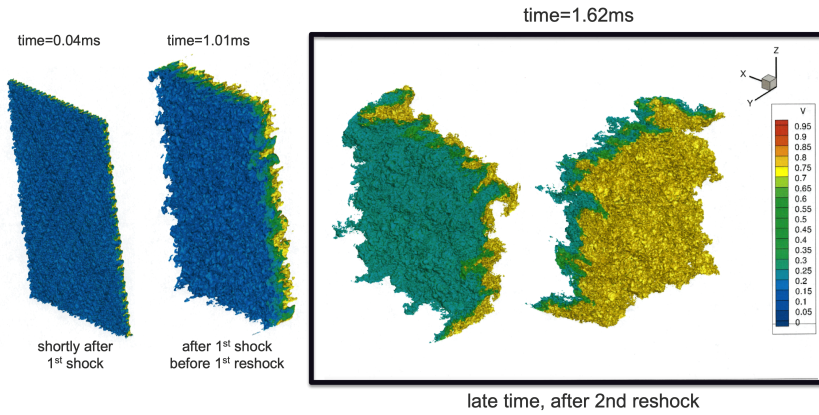


Figure 1.17 SF_6 mass-fraction isosurface visualizations of 0.05 mm resolution LMC-xRAGE LES predictions. Reprinted from Grinstein (2024), with permission from Elsevier.

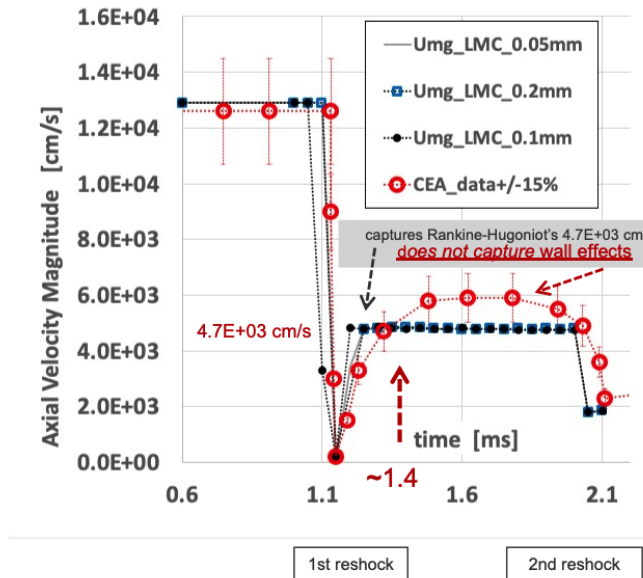


Figure 1.18 Axial velocity magnitude at $x = 161$ mm, LMC-xRAGE LES vs. laboratory data. Reprinted from Grinstein (2024), with permission from Elsevier.

associated with the reflected shocks. Laboratory transverse velocity variance (R22) data was reported at the location 169 mm (Mugler and Gauthier, 2000; Grégoire et al., 2005). At the location 161 mm – just after the first reshock, Figure 1.19 shows a strong increase of the axial velocity variance was observed reaching a peak laboratory value of $117(m/s)^2$, as the axial variance in the gaseous mixture has been excited by the first-reflected shock. Our results for R11 are consistent with those reported in the laboratory experiments – particularly so immediately after the first reshock (finest 0.1 mm and 0.05 mm resolution LMC-xRAGE LES

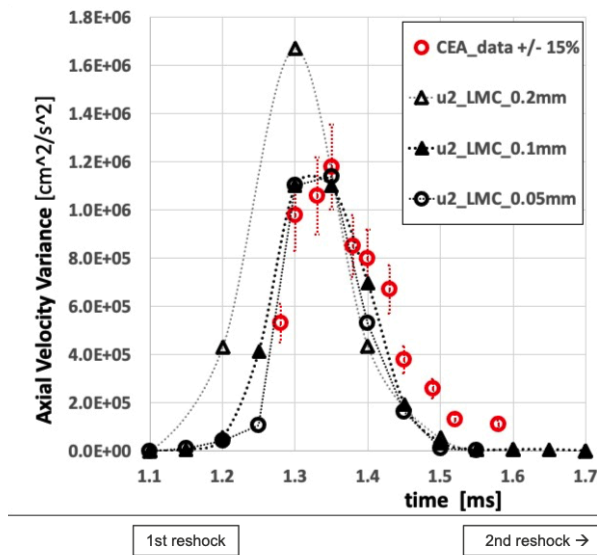


Figure 1.19 Axial velocity variance at $x = 161$ mm, LMC-xRAGE LES vs. laboratory data. Reprinted from Grinstein (2024), with permission from Elsevier.

results fall within reported $\pm 15\%$ uncertainty bar at the location 161 mm), and are fairly stable as a function of grid resolution changes also for R22 (Grinstein et al., 2021). The highest values for R11 occur mostly just after the first reshock as in Poggi et al. (1998). The peak R22 values quoted in Mugler and Gauthier (2000) and Grégoire et al. (2005) are fractions $\sim 1/3$ of their R11 counterparts – which is also consistent with our findings.

1.5.3 Dynamic Bridging Mixing Validated with LES

As in Grinstein et al. (2020), our 3D Dynamic BHR simulations in this work use $q_{ij} = T_{ij}$ in conjunction with $l = 2$. We used between 2 and 8 levels of AMR with the finest resolutions ranging between 0.2 mm and 0.05 mm, respectively. More practically motivated Dynamic BHR bridging simulations used 2–4 levels of AMR with the finest 0.100 mm resolution. The shock-tube simulations used between 0.1 and 5.5×10^9 computational cells.

Mixing measures less sensitive to SGS contributions may enable accurate prediction of quantities of interest with the bridging-based generated LES with less resolution than required with the LES high-fidelity option. Such potential benefits were noted in (Grinstein et al., 2020) with regard to having scalar-mixing predictions converged on coarser grids with the more accurate LMC xRAGE. We examined the impact of bridging length L choices in this context.

Figure 1.20 shows the center plane predicted mass-fraction distributions associated with dynamic bridging and LMC-xRAGE LES for the coarsest 0.2 mm resolution (two-level AMR) case. Prediction accuracy is determined by the ability to capture the vortical structures responsible for the onset and development of turbulence, and bridging modeling efficiency is directly determined by how much *less* resolution is required to resolve the flow scales not

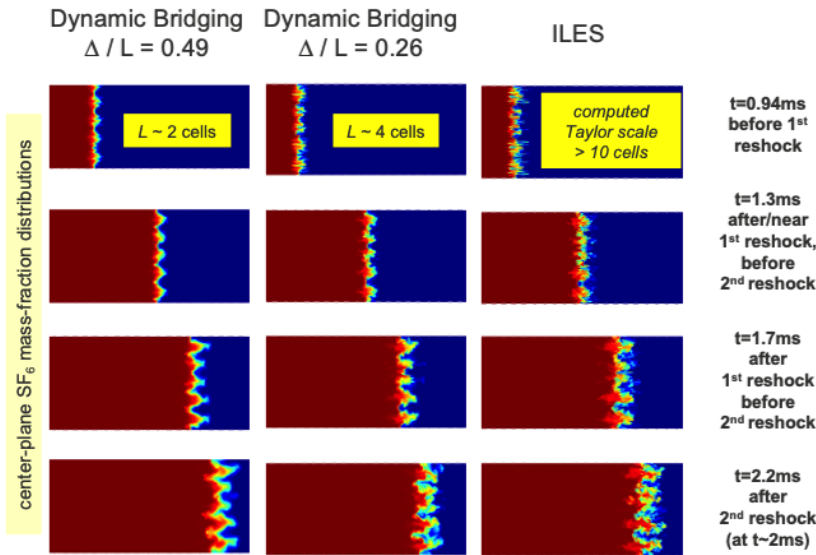


Figure 1.20 Dynamic BHR vs. LES for 0.2 mm resolution (two-level AMR). Reprinted from Grinstein (2024), with permission from Elsevier.

amenable to modeling (Pereira et al., 2018). Results with bridging length $L \sim 2$, and $L \sim 4$ (smallest) cells are shown at selected times before, after, and between the reshock events.

Varying the bridging length directly impacts the detailed captured content of space/time fluctuations effects with Dynamic BHR. Figure 1.21 shows probability distribution functions (PDF’s) of the contribution function f over the whole 3D domain versus $\Delta x/L$. Significantly smaller values ($f \sim 0.1\text{--}0.3$) indicate less contribution of RANS for $\Delta x/L = 0.26$, consistent with the corresponding results in Figure 1.20 – for which case increased captured content of space/time fluctuations effects are depicted. The suitability of this $\Delta x/L$ *sweet spot* value is confirmed below in terms of results for the *chevron* shock-tube case.

For the sake of quantitative mix analysis, we consider here a frequently used integrated mixing measure (Hahn et al., 2011), $TMX = 4 \int \bar{\rho}^2 \bar{Y}_{air} \bar{Y}_{SF_6} dx$, in terms of the mass density ρ , SF_6 and air mass fractions Y_{SF_6} and $Y_{air} = 1 - Y_{SF_6}$, and using transverse-plane averaging, $\bar{\phi}(x) = \int \phi(x, y, z) dydz / \int dydz$.

The top portion of Figure 1.22 compares TMX versus resolution and bridging length L . The ability of the dynamic bridging model to capture the basic mixing features with less resolution is well apparent between first and second reshock, where the 0.2 mm and 0.1 mm bridging predictions for $\Delta/L = 0.26$ are in very good agreement with the finest (0.05 mm) LES – suggesting preferred bridging/resolution trade-offs and robust mixing capturing with coarser gridding. Accurate mixing predictions can be thus attained with dynamic BHR with significantly less resolution than required with the highest-fidelity turbulence simulation models typically used at scale with default xRAGE hydrodynamics (Grinstein et al., 2021). Two levels of grid-coarsening savings are achieved for the improved mixing predictions: one

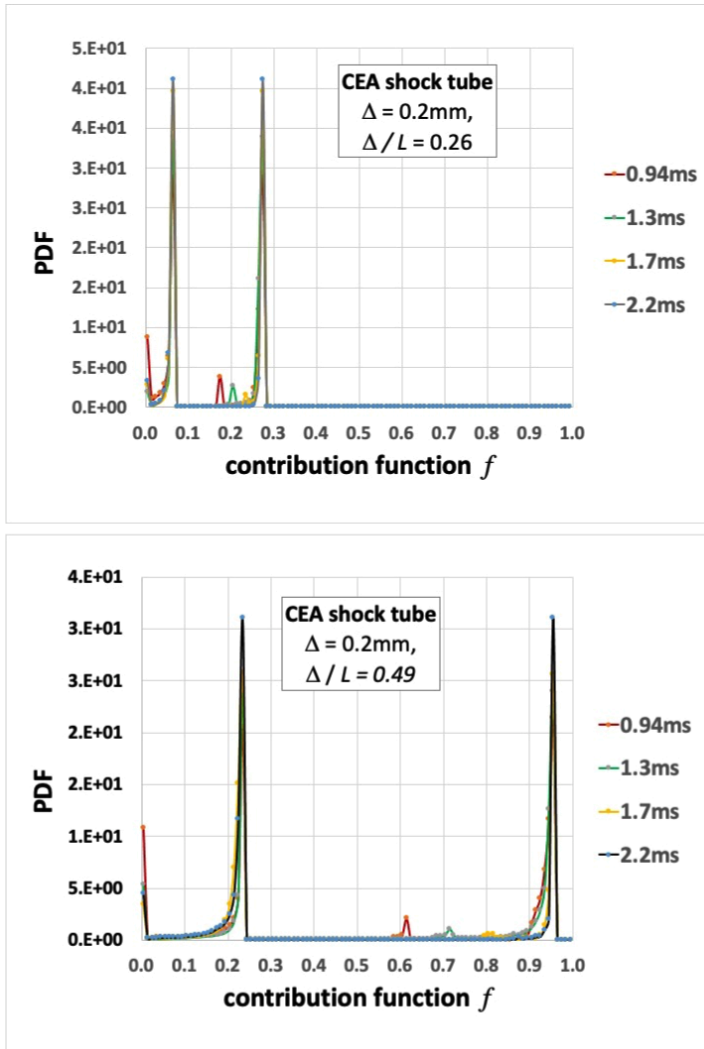


Figure 1.21 Dynamic BHR shock-tube simulations; PDF of the contribution function vs. $\Delta x/L$. Reprinted from Grinstein (2024), with permission from Elsevier.

associated with the more accurate LMC-xRAGE hydrodynamics and an additional one from using the dynamic xRAGE-BHR bridging.

Beyond the second reshock, bridging with 0.1 mm resolution and $\Delta/L = 0.26$ still provides good predictions – albeit RANS corrections to better converged (resolved) LES appear unnecessary there. This is confirmed in the bottom part of Figure 1.22, where the focus is on the case $\Delta/L = 0.26$, and on examining dynamic BHR simulations restarted at time 1.65 ms (before 2nd reshock) and continued thereafter with RANS contributions turned off (i.e., pure ILES); significantly improved mixing predictions are thus achieved after second reshock for both resolutions. The latter results suggest potential benefits of imposing additional late-time constraints on f , for example, by requiring that f vanish at late-times when conditions are met

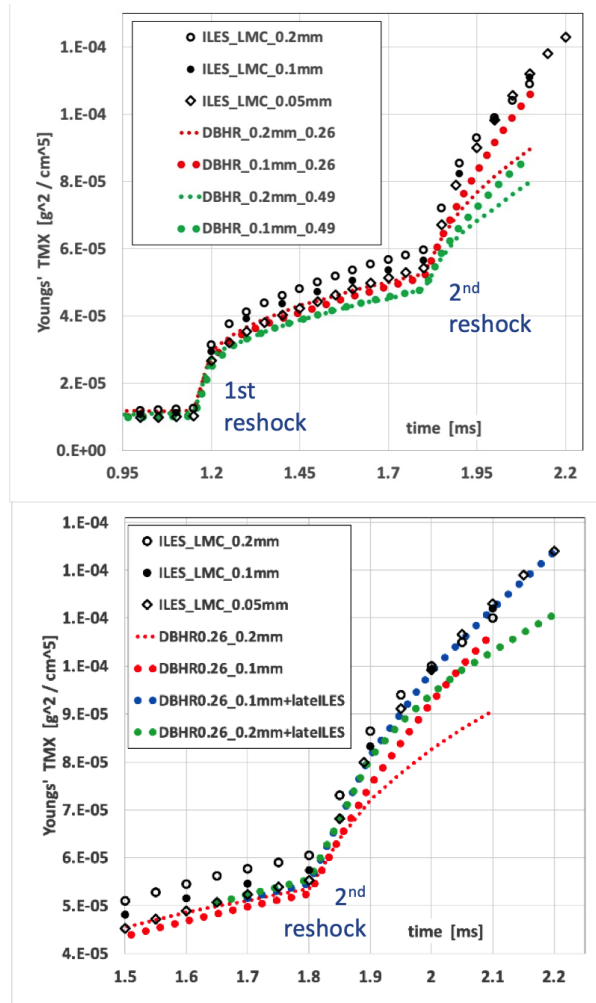


Figure 1.22 TMX for LMC-xRAGE LES and Dynamic BHR vs. resolution for $\Delta/L = 0.26, 0.49$ (top); for $\Delta/L = 0.26$, results for dynamic BHR + late-time LES are also included (pure LES after time 1.65 ms) – focusing on improved mixing prediction after second reshock (bottom). Reprinted from Grinstein (2024), with permission from Elsevier.

in terms of a suitable progress variable characterizing transition and small-scale population – for example, as a function of λ_c .

On separate notes (Grinstein et al., 2021; Grinstein, 2024), the axial velocity variance results between the first and second reshock exhibited similar velocity turbulence features captured with dynamic bridging and ILES as a function of grid resolution, indicating that the dynamic bridging modeling does not appear to provide much added improvement on the turbulent velocity fluctuations predictions for a given resolution. This suggests that exploring the use of an explicit SGS component in (1.20) using the extended dynamic bridging formalism in Grinstein et al. (2021) may be warranted for the coarsest grid resolutions.

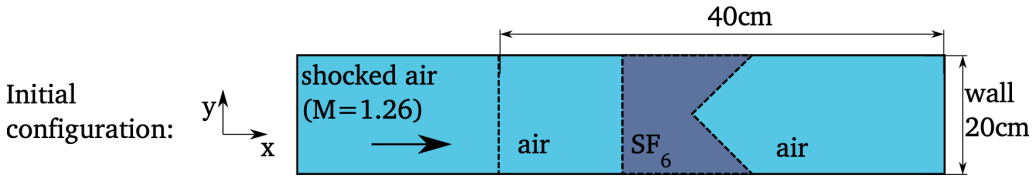


Figure 1.23 Schematic of the chevron shock tube. Reprinted from Grinstein (2024), with permission from Elsevier.

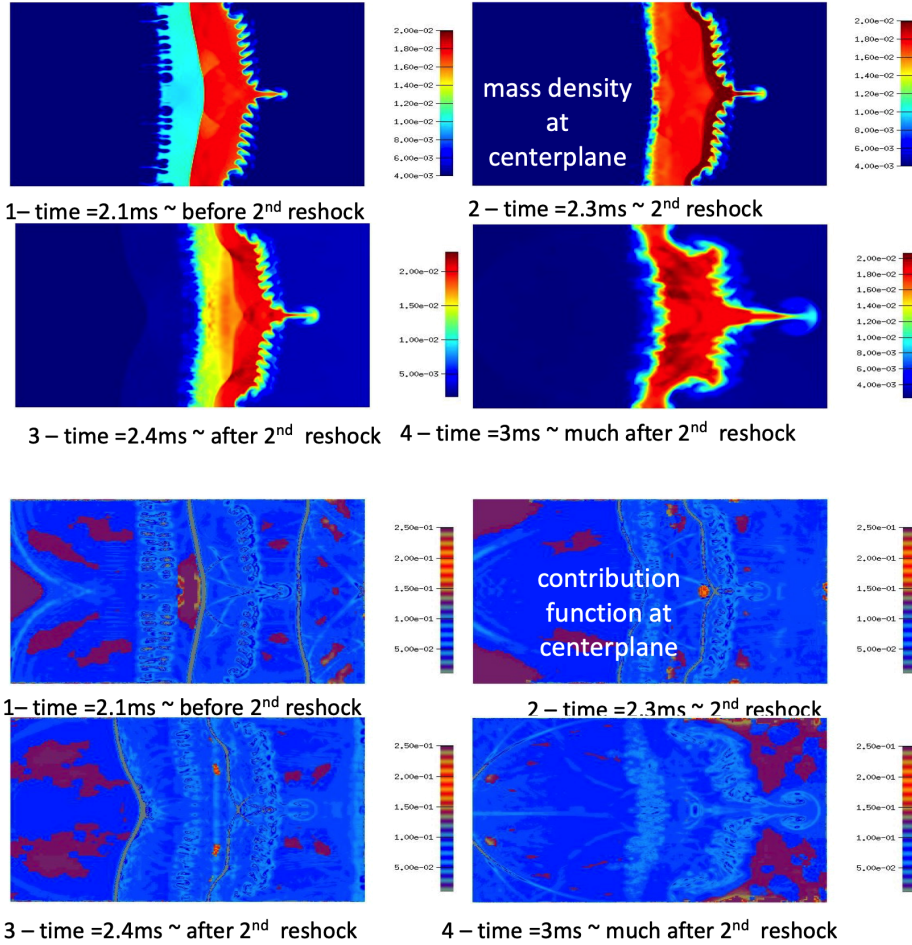


Figure 1.24 Chevron shock-tube Dynamic BHR simulation center plane mass-fraction visualization results for $\Delta/L = 0.25$. Reprinted from Grinstein (2024), with permission from Elsevier.

Contribution Function Analysis for the Chevron Shock Tube

The *chevron* shock-tube case (Hahn et al., 2011) – involving high (SF_6) and low (air) density gases initially separated by membranes and wire mesh is indicated schematically in Figure

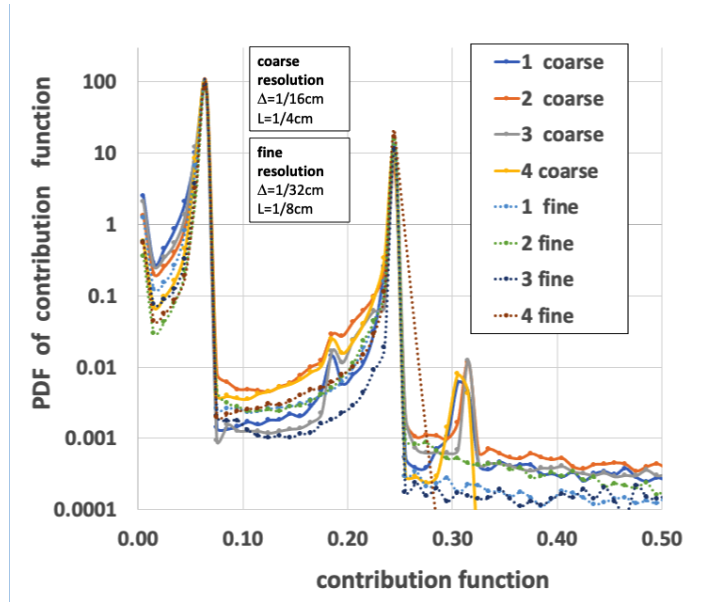


Figure 1.25 Chevron shock-tube Dynamic BHR simulations; PDF of the contribution function for $\Delta/L = 0.25$. Reprinted from Grinstein (2024), with permission from Elsevier.

1.23. The growth of the RMI and characteristic turbulent mixing measures are studied using interface perturbations involving prescribed spectral content and standard deviation $s.d.$ The SF_6 and air are assumed to be initially in temperature and pressure equilibrium at 1 bar, with densities of 6.34 kg/m^3 and 1.184 kg/m^3 , respectively. A shocked air region is created upstream in terms of a higher-density higher-pressure region chosen to satisfy the Rankine–Hugoniot relations for a $Ma = 1.26$ shock. The shock propagates in the (x) direction through the contact discontinuity and reflects at the right (reflective) boundary. Uniform cartesian gridding with smallest grid sizes Δ of $1/16 \text{ cm}$ and $1/32 \text{ cm}$ were employed in our earlier *chevron* simulations (Haines et al., 2013; Grinstein et al., 2019, 2020) having $\Delta/L = 0.21, 0.10$. AMR with grid sizes ranging between ($1/4 \text{ cm} - 1/16 \text{ cm}$) and ($1/4 \text{ cm} - 1/32 \text{ cm}$) and fixed $\Delta/L = 0.25$ were considered.

Representative temporal evolution of center plane visualizations of SF_6 mass-fraction and f distributions are shown in Figure 1.24. Corresponding full-domain PDFs of f for the selected times and both grid resolutions presented in Figure 1.25 indicate relatively small RANS contributions ($f < 0.3$) for $\Delta/L = 0.25$ – consistent with $\Delta/L = 0.26$ being a convenient working choice for Dynamic BHR for the planar shock-tube case. Finally, sensitivities to grid resolution shown in Figure 1.26 clearly depict the robustness of the late-time mixing predictions.

1.6 Outlook

Throughout our presentation, we have emphasized the inherently intrusive nature of coarse-grained observations in computational and laboratory experiments, intimately linked to

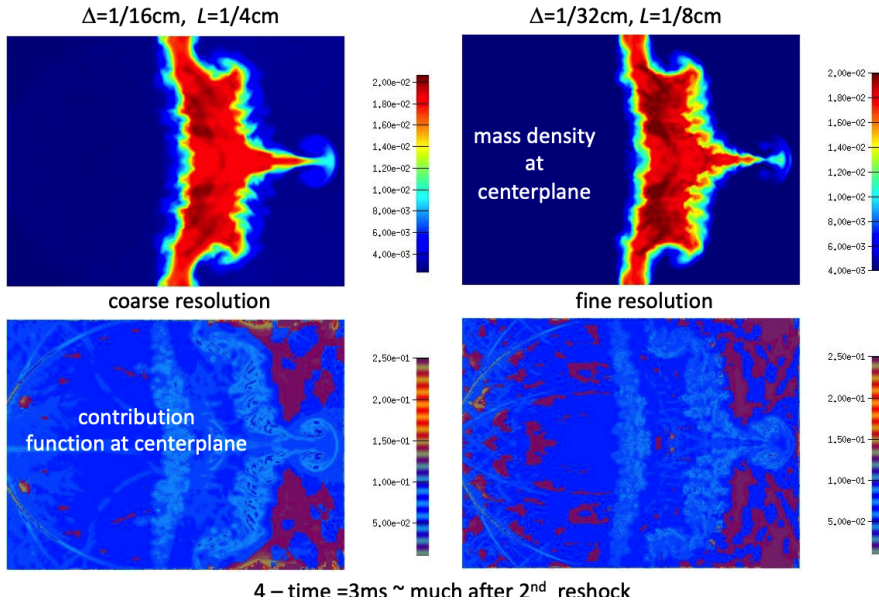


Figure 1.26 Chevron shock-tube Dynamic BHR simulations center plane mass-fraction visualizations, late-time ($t = 3.09$ ms) sample results vs. grid resolution for $\Delta/L = 0.25$. Reprinted from Grinstein (2024), with permission from Elsevier.

their SGS and SPG specifics. Difficult challenges are then related to characterizing and modeling unresolved SGS and SPG aspects and assessing uncertainties associated with CG predictions and laboratory measurements. Suitable verification, validation, and uncertainty quantification processes provide a rational basis to decide on CG modeling goodness for its intended purpose. Issues of SGS modeling have motivated intense research in the last four decades. Late-time (or far-field) sensitivity of observations to (SPG) initial and other boundary conditions has also been recognized as a crucial aspect to be addressed.

Nondissipative SGS issues are presumably less important for high enough Re (large scale separation) but need to be carefully addressed when relatively short-scale separations are involved. Largely uncharacterized small-scale turbulence processes remain in the turbulent variable-density context, including: effects of SGS perturbations to initial material interfaces; effects of interacting shocks and sharp material interfaces with turbulence; baroclinic production of vorticity and other effects of small-scale density variations; exothermicity effects of chemical (or thermonuclear) reactions resulting from molecular scale material mixing.

Robust CG simulations for dissipative turbulent phenomena exhibiting enslavement of small-scale dynamics are, in principle, achievable with suitable SGS modeling, enough scale separation, and well-resolved IC. However, predictability assessments for high- Re phenomena cannot be robust when inherent resolution sensitivities are present – while nature controls the flow physics independently. *If the initial conditions content in filtered-out smaller and SGS spatial scales can significantly alter the evolution of the larger scales of motion and practical integral measures, then the use of any CG strategy for their prediction is dubious and not rationally or scientifically justifiable* (Grinstein, 2009). These are serious

concerns when coarse-grained observations are constrained by characterization and modeling of intertwined SGS and SPG specifics.

Turbulent mixing modeling and predictability rely on the availability of big data from computational and laboratory experiments. Fundamental issues of big data generation involve characterizing and modeling the specific flow conditions at the SGS and SPG scales. Big data purpose, generation, reduction, and organization are qualified by the very specific research questions of interest to be addressed and by the predictability metrics in the associated verification, validation, and uncertainty quantification process. In practice, only certain statistical predictions and big data types will be useful. Ensemble averaging solutions over a suitably complete set of realizations covering initial conditions (and other) relevant variability remains a data reduction strategy of choice.

Acknowledgments

Los Alamos National Laboratory is operated by TRIAD National Security, LLC for the US DOE NNSA under contract 89233218CNA000001.

References

- Anderson, J. D. 1998. *A History of Aerodynamics*. 1st ed. Cambridge University Press.
- Balachandar, S. 2024. *Fundamentals of Dispersed Multiphase Flows*. Cambridge University Press.
- Balakumar, B. J., Orlicz, G. C., Tomkins, C. D., and Prestridge, K. P. 2008. Simultaneous Particle-Image Velocimetry-Planar Laser-Induced Fluorescence Measurements of Richtmyer–Meshkov Instability Growth in a Gas Curtain with and without Reshock. *Physics of Fluids*, **20**(124103).
- Balasubramanian, S., Orlicz, G. C., Prestridge, K. P., and Balakumar, B. J. 2012. Experimental Study of Initial Condition Dependence on Richtmyer–Meshkov Instability in the Presence of Reshock. *Physics of Fluids*, **24**, 034103.
- Besnard, D., Harlow, F. H., Rauenzahn, R. M., and Zemach, C. 1992. *Turbulence Transport Equations for Variable-Density Turbulence and Their Relationship to Two-Field Models*. Technical Report LA-UR-92-12303. Los Alamos National Laboratory, Los Alamos, USA.
- Blaisdell, G. A., Mansour, N. N., and Reynolds, W. C. 1994. Compressibility Effects on the Passive Scalar Flux within Homogeneous Turbulence. *Physics of Fluids*, **6**, 3498–3500.
- Book, D. L., Li, C., Patnaik, G., and Grinstein, F. F. 1991. Quantifying Residual Numerical Diffusion in Flux-Corrected Transport Algorithms. *Journal of Scientific Computing*, **6**, 323–343.
- Boris, J. P. 1990. On Large Eddy Simulation Using Subgrid Turbulence Models. Pages 344–353 of: *Whither Turbulence? Turbulence at the Crossroads*, Lumley, J. L. (ed). Springer.
- Boris, J. P., Grinstein, F. F., Oran, E. S., and Kolbe, R. L. 1992. New Insights into Large Eddy Simulation. *Fluid Dynamics Research*, **10**(4–6), 199–228.
- Bose, S. T., Moin, P., and You, D. 2010. Grid-Independent Large-Eddy Simulation Using Explicit Filtering. *Physics of Fluids*, **22**, 105103.
- Box, G. E. P. 1979. Robustness in the Strategy of Scientific Model Building. Pages 201–236 of: *Robustness in Statistics*, Launer, R. L., and Wilkinson, G. N. (eds). Academic Press.
- Brachet, M. E., Meiron, D. I., Orzag, S. A., Nickel, B. G., Morf, R. H., and Frisch, U. 1983. Small Scale Structure of the Taylor–Green Vortex. *Journal of Fluid Mechanics*, **130**, 411–452.
- Brouillette, M. 2002. The Richtmyer–Meshkov Instability. *Annual Review of Fluid Mechanics*, **34**, 445–468.
- Celik, I., Klein, M., Freitag, M., and Janicka, J. 2006. Assessment Measures for URANS/DES/LES: An Overview with Applications. *Journal of Turbulence*, **7**, N48.

- Cohen, R. H., Dannevik, W. P., Dimits, A. M., Eliason, D. E., Mirin, A. A., Zhou, Y., Porter, D. H., and Woodward, P. R. 2002. Three-Dimensional Simulation of a Richtmyer–Meshkov Instability with a Two-Scale Initial Perturbation. *Physics of Fluids*, **14**, 3692–3709.
- Colella, P. 1982. Glimm’s Method for Gas Dynamics. *SIAM Journal on Scientific and Statistical Computing*, **3**(1), 76–110.
- Colella, P., and Woodward, P. R. 1984. The Piecewise Parabolic Method (PPM) for Gas-Dynamical Simulations. *Journal of Computational Physics*, **54**(1), 174–201.
- Davidson, P. A. 2006. *Turbulence: An Introduction for Scientists and Engineers*. Oxford University Press.
- Dimotakis, P. E. 2000. The Mixing Transition in Turbulent Flows. *Journal of Fluid Mechanics*, **409**, 69–98.
- Domaradzki, J. A., and Adams, N. A. 2002. Direct Modeling of Subgrid Scales of Turbulence in Large Eddy Simulations. *Journal of Turbulence*, **3**(24), 1–19.
- Domaradzki, J. A., Xiao, Z., and Smolarkiewicz, P. 2003. Effective Eddy Viscosities in Implicit Large Eddy Simulations of Turbulent Flows. *Physics of Fluids*, **15**, 3890–3893.
- Drikakis, D., Fureby, C., Grinstein, F. F., and Youngs, D. 2007. Simulation of Transition and Turbulence Decay in the Taylor–Green Vortex. *Journal of Turbulence*, **8**(20).
- Druault, P., Lardeau, S., Bonnet, J. P., F. Coiffet, F., Delville, J., Lamballais, E., Largeau, J. F., and Perret, L. 2004. Generation of Three-Dimensional Turbulent Inlet Conditions for Large-Eddy Simulation. *AIAA Journal*, **42**, 447–456.
- Fan, M., Wenren, Y., Dietz, W., Xiao, M., and Steinhoff, J. 2002. Computing Blunt Body Flows on Coarse Grids Using Vorticity Confinement. *Journal of Fluids Engineering*, **124**(4), 876–885.
- Fasel, H. F., and von Terzi, D. A. 2006. A Methodology for Simulating Compressible Turbulent Flows. *J. Appl. Mech.*, **73**, 405–12.
- Frisch, U. 1995a. *Turbulence: The Legacy of A. N. Kolmogorov*. Cambridge University Press.
- Frolich, J., and von Terzi, D. A. 2008. Hybrid LES/RANS Methods for the Simulation of Turbulent Flows. *Progress in Aerospace Sciences*, **44**, 349–77.
- Fureby, C. 2009. LES Modeling of Combustion for Propulsion Applications. *Philosophical Transactions of the Royal Society A*, **367**, 2957–2969.
- Fureby, C., and Grinstein, F. F. 2002. Large Eddy Simulation of High-Reynolds-Number Free and Wall-Bounded Flow. *Journal of Computational Physics*, **181**(1), 68–97.
- Fureby, C., and Grinstein, F. F. 1999. Monotonically Integrated Large Eddy Simulation of Free Shear Flows. *AIAA Journal*, **37**(5), 544–556.
- Fureby, C., and Tabor, G. 1997. Mathematical and physical constraints on large-eddy simulations. *Theor. Computational Fluid Dynamics*, **9**, 85–102.
- George, W. K., and Davidson, L. 2004a. Role of Initial Conditions in Establishing Asymptotic Flow Behavior. *AIAA Journal*, **42**, 438–446.
- George, W. K. 1989. The Self-Preservation of Turbulent Flows and its Relation to Initial Conditions and Coherent Structures. In: *Advances in Turbulence*, George, W. K., and Arndt, R. E. A. (eds). Hemisphere Press.
- George, W. K. 1990. Governing Equations, Experiments, and the Experimentalist. *Experimental Thermal and Fluid Science*, **3**, 557–566.
- George, W. K., and Davidson, L. 2004b. Role of Initial Conditions in Establishing Asymptotic Flow Behavior. *AIAA Journal*, **42**(3), 438–446.
- George, W. K., and Tutkun, M. 2009. Mind the Gap: A Guideline for Large Eddy Simulation. *Philosophical Transactions of the Royal Society A*, **1899**, 2839–47.
- Germano, M. 1992. The Filtering Approach. *Journal of Fluid Mechanics*, **238**, 325–36.
- Germano, M. 1998. Readers’ Forum, Comment on Turbulence Modeling for Time-Dependent RANS and VLES: A Review. *AIAA Journal*, **36**(9), 1766–1767.
- Germano, M. 2007. A Direct Relation between the Filtered Subgrid Stress and the Second Order Structure Function. *Physics of Fluids*, **19**, 038102/2.
- Ghosal, S. 1996. An Analysis of Numerical Errors in Large-Eddy Simulations of Turbulence. *Journal of Computational Physics*, **125**(1), 187–206.

- Gittings, M., Weaver, R., Clover, M., Betlach, T., Byrne, N., Coker, R., Dendy, E., Hueckstaedt, R., New, K., Oakes, W. R., Ranta, D., and Stefan, R. 2008. The RAGE Radiation-Hydrodynamic Code. *Computational Science & Discovery*, **1**(1), 015005.
- Gotoh, T., and Watanabe, T. 2012. Scalar Flux in a Uniform Mean Scalar Gradient in Homogeneous Isotropic Steady Turbulence. *Physica D*, **241**, 141–148.
- Gowardhan, A. A., and Grinstein, F. F. 2011. Numerical Simulation of Richtmyer–Meshkov Instabilities in Shocked Gas Curtains. *Journal of Turbulence*, **12**(43), 1–24.
- Gowardhan, A. A., Ristorcelli, J. R., and Grinstein, F. F. 2011. The Bipolar Behavior of the Richtmyer–Meshkov Instability. *Physics of Fluids Letters*, **23**(071701).
- Grinstein, F. F. 1995. Self-Induced Vortex Ring Dynamics in Subsonic Rectangular Jets. *Physics of Fluids*, **7**(10), 2519–2521.
- Grinstein, F. F. 2001. Vortex Dynamics and Entrainment in Rectangular Free Jets. *Journal of Fluid Mechanics*, **437**, 69–101.
- Grinstein, F. F. 2004. Boundary Conditions for Large Eddy Simulation. *AIAA Journal Special Section*, **42**, 437–492.
- Grinstein, F. F. 2009. On Integrating Large Eddy Simulation and Laboratory Turbulent Flow Experiments. *Philosophical Transactions of the Royal Society A*, **367**, 2931–2945.
- Grinstein, F. F. 2010. Vortex Dynamics and Transition in Free Shear Flows. Chap. 8 of: *ILES: Computing Turbulent Fluid Dynamics*, Grinstein, F. F., Margolin, L. G., and Rider, W. J. (eds). Cambridge University Press.
- Grinstein, F. F. 2016. *Coarse Grained Simulation and Turbulent Mixing*. Cambridge University Press.
- Grinstein, F. F. 2017. Initial Conditions and Modeling for Simulations of Shock Driven Turbulent Material Mixing. *Computers and Fluids*, **151**, 58–72.
- Grinstein, F. F. 2020. Coarse Grained Simulation of Convectively Driven Turbulent Mixing, Transition, and Turbulence Decay. *Physica D: Nonlinear Phenomena*, **407**, 132419.
- Grinstein, F. F. 2024. Coarse Grained Simulation and Dynamic Bridging for Turbulent Mixing Predictions. *Computers and Fluids*, **271**, 106185.
- Grinstein, F. F., and Fureby, C. 2007. On Flux-Limiting-Based Implicit Large Eddy Simulation. *Journal of Fluids Engineering*, **129**(12), 1483–1492.
- Grinstein, F. F., Margolin, L. G., and Rider, W. J. 2010. *Implicit Large Eddy Simulation: Computing Turbulent Flow Dynamics*. 2nd ed. Cambridge University Press.
- Grinstein, F. F., Gowardhan, A. A., and Wachtor, A. J. 2011. Simulations of Richtmyer–Meshkov Instabilities in Planar Shock-Tube Experiments. *Physics of Fluids*, **23**(034106).
- Grinstein, F. F., Saenz, J. A., Dolence, J. C., Masser, T. O., Rauenzahn, R. M., and Francois, M. M. 2019. Effects of Operator Splitting and Low Mach-Number Correction in Turbulent Mixing Transition Simulations. *Computers and Mathematics with Applications*, **78**(2), 437–458.
- Grinstein, F. F., Saenz, J. A., Rauenzahn, R. M., Germano, M., and Israel, D. M. 2020. Dynamic Bridging Modeling for Coarse Grained Simulations of Shock Driven Turbulent Mixing. *Physics of Fluids*, **199**, 104430.
- Grinstein, F. F., Saenz, J. A., and Germano, M. 2021. Coarse Grained Simulations of Shock-Driven Turbulent Material Mixing. *Physics of Fluids*, **33**(035131).
- Grinstein, F. F., Pereira, F. S., and Rider, W. J. 2023. Numerical Approximations Formulated as LES Models. Chap. 10 of: *Numerical Methods in Turbulence Simulations*, Moser, R. (ed). Elsevier.
- Grégoire, O., Souffland, D., and Gauthier, S. 2005. A Second-Order Turbulence Model for Gaseous Mixtures induced by Richtmyer–Meshkov Instability. *Journal of Turbulence*, **6**(1).
- Guillard, H., and Murrone, A. 2004. On the Behavior of Upwind Schemes in the Low Mach Number Limit: II. Godunov Type Schemes. *Computers & Fluids*, **33**(4), 655–675.
- Gutmark, E., and Ho, C. M. 1983. Preferred Modes and the Spreading Rates of Jets. *Physics of Fluids*, **26**, 2932.
- Hahn, M., Drikakis, D., Youngs, D. L., and Williams, R. J. R. 2011. Richtmyer–Meshkov Turbulent Mixing Arising from an Inclined Material Interface with Realistic Surface Perturbations and Reshocked Flow. *Physics of Fluids*, **23**, 046101.

- Haines, B. M., Grinstein, F. F., and Schwarzkopf, J. D. 2013. Reynolds-Averaged Navier–Stokes Initialization and Benchmarking in Shock-Driven Turbulent Mixing. *Journal of Turbulence*, **14**(2), 46–70.
- Haines, B. M., Grinstein, F. F., and Fincke, J. R. 2014. Three-Dimensional Simulation Strategy to Determine the Effects of Turbulent Mixing on Inertial-Confinement-Fusion Capsule Performance. *Physical Review E*, **89**(5).
- Harten, A., Lax, P. D., and van Leer, B. 1983. On Upstream Differencing and Godunov-Type Schemes for Hyperbolic Conservation Laws. *SIAM Review*, **25**(1), 35–61.
- Heisenberg, W. 1958. *Physics and Philosophy: The Revolution in Modern Science*. Harper & Row.
- Hill, D. J., Pantano, C., and Pullin, D. I. 2006. Large-Eddy Simulation and Multiscale Modelling of a Richtmyer–Meshkov Instability with Reshock. *Journal of Fluid Mechanics*, **557**, 29–61.
- Hirt, C. W. 1969. Computer Studies of Time-Dependent Turbulent Flows. *Physics of Fluids*, **12**(12), II–219–II–227.
- Hussain, A. K. M. F., and Husain, H. S. 1989. Elliptic Jets. Part I. Characteristics of Unexcited and Excited Jets. *Journal of Fluid Mechanics*, **208**, 257–320.
- Hussain, A. K. M. F., and Reynolds, W. C. 1970. The Mechanics of an Organized Wave in Turbulent Shear Flow. *Journal of Fluid Mechanics*, **41**(2), 241–258.
- Hussain, A. K. M. F., and Zedan, M. F. 1978. Effects of the Initial Condition on the Axisymmetric Free Shear Layer: Effect of the Initial Fluctuation Level. *Physics of Fluids*, **21**, 1475–81.
- Jiménez, J., Wray, A. A., Saffman, P. G., and Rogallo, R. S. 1993. The Structure of Intense Vorticity in Isotropic Turbulence. *Journal of Fluid Mechanics*, **255**, 6590.
- Kaneda, Y., Ishihara, T., Yokokawa, M., Itakura, K., and Uno, A. 2003. Energy Dissipation Rate and Energy Spectrum in High Resolution Direct Numerical Simulations of Turbulence in a Periodic Box. *Physics of Fluids*, **15**(2), L21–L24.
- Karamanos, G.-S., and Karniadakis, G. E. 2000. A Spectral Vanishing Viscosity Method for Large-Eddy Simulations. *Journal of Computational Physics*, **163**, 22–50.
- Kokkinakis, I. W., and Drikakis, D. 2015. Implicit Large Eddy Simulation of weakly compressible turbulent channel flow. *Computer Methods in Applied Mechanics and Engineering*, **287**, 229–261.
- Leinov, E., Malamud, G., Elbaz, Y., Levin, A., Ben-dor, G., Shvarts, D., and Sadot, O. 2009. Experimental and Numerical Investigation of the Richtmyer–Meshkov Instability under Reshock Conditions. *Journal of Fluid Mechanics*, **626**(449–75).
- Leonard, A. 1975. Energy Cascade in Large-Eddy Simulations of Turbulent Fluid Flows. *Adv. in Geophysics*, **18A**, 237–248.
- Lesieur, M. 2008. *Turbulence in Fluids*. Springer.
- Leweke, T., Dizés, S. Le, and Williamson, C. H. K. 2016. Dynamics and Instabilities of Vortex Pairs. *Annual Review of Fluid Mechanics*, **48**(1), 507–541.
- Li, G., and Gutmark, E. J. 2006. Experimental Study of Boundary Condition Effects on Non-Reacting and Re-Acting Flow in a Multi-Swirl Gas Turbine Combustor. *AIAA Journal*, **44**, 444.
- Lorenz, E. N. 1963. Deterministic Nonperiodic Flow. *Journal of Atmospheric Sciences*, **3**, 130–141.
- Margolin, L. G. 2009. Finite-Scale Equations for Compressible Fluid flow. *Phil. Trans. R. Soc. A*, **367**, 2861–71.
- Margolin, L. G., and Rider, W. J. 2002. A Rationale for Implicit Turbulence Modeling. *International Journal of Numerical Methods in Fluids*, **39**, 821–41.
- Margolin, L. G., Rider, W. J., and Grinstein, F. F. 2006. Modeling Turbulent Flow with Implicit LES. *Journal of Turbulence*, **7**(N15), 1–27.
- Margolin, L. G., and Rider, W. J. 2010. Numerical Regularization: The Numerical Analysis of Implicit Subgrid Models. Chap. 5 of: *ILES: Computing Turbulent Fluid Dynamics*, Grinstein, F. F., Margolin, L. G., and Rider, W. J. (eds). Cambridge University Press.
- Misra, A., and Pullin, D. I. 1997. A Vortex-Based Subgrid Stress Model for Large-Eddy Simulation. *Physics of Fluids*, **9**, 2443.
- Moore, W. C., and Balachandar, S. 2019. Lagrangian Investigation of Pseudo-Turbulence in Multiphase Flow Using Superposable Wakes. *Physical Review Fluids*, **4**, 114301.
- Moser, R. D., Haering, S. W., and Yalla, G. R. 2021. Statistical Properties of Subgrid-Scale Turbulence Models. *Annual Reviews of Fluid Mechanics*, **53**, 255–286.

- Mugler, C., and Gauthier, S. 2000. Two-Dimensional Navier–Stokes Simulations of Gaseous Mixtures Induced by Richtmyer–Meshkov Instability. *Physics of Fluids*, **12**, 1783.
- Orlicz, G. C., Balakumar, B. J., Tomkins, C. D., and Prestridge, K. P. 2009. A Mach Number Study of the Richtmyer–Meshkov Instability in a Varicose, Heavy-Gas Curtain. *Physics of Fluids*, **21**(064102).
- Overholt, M. R., and Pope, S. B. 1996. Direct Numerical Simulation of a Passive Scalar with Imposed Mean Gradient in Isotropic Turbulence. *Physics of Fluids*, **8**, 3128–3148.
- Parish, E. J., and Duraisamy, K. 2017. Non-Markovian Closure Models for Large Eddy Simulations Using the Mori–Zwanzig Formalism. *Physical Review Fluids*, **2**, 014604.
- Patnaik, G., Boris, J. P., Young, T. R., and Grinstein, F. F. 2007. Large Scale Urban Contaminant Transport Simulations with MILES. *Journal of Fluids Engineering*, **129**, 1524–1532.
- Pereira, F. S., Eça, L., Vaz, G., and Girimaji, S. S. 2018. Challenges in Scale-Resolving Simulations of Turbulent Wake Flows with Coherent Structures. *Journal of Computational Physics*, **363**, 98–115.
- Pereira, F. S., Eça, L., Vaz, G., and Girimaji, S. S. 2019. On the Simulation of the Flow Around a Circular Cylinder at $Re = 140,000$. *International Journal of Heat and Fluid Flow*, **76**, 40–56.
- Pereira, F. S., Grinstein, F. F., and Israel, D. 2020. Effect of the Numerical Discretization Scheme in Shock-Driven Turbulent Mixing. *Computers and Fluids*, **201**(104487).
- Pereira, F. S., Grinstein, F. F., Israel, D. M., and Rauen Zahn, R. 2021. Molecular Viscosity and Diffusivity Effects in Transitional and Shock-Driven Mixing Flows. *Physical Review E*, **103**, 013106.
- Pereira, F. S., Grinstein, F. F., Israel, D. M., and Eça, L. 2022. Verification and Validation: The Path to Predictive Scale-Resolving Simulations of Turbulence. *ASME Journal of Verification, Validation, and Uncertainty Quantification*, **7**(2), 021003.
- Poggi, F., Thoremby, M.-H., and Rodriguez, G. 1998. Velocity Measurements in Turbulent Gaseous Mixtures Induced by Richtmyer–Meshkov Instability. *Physics of Fluids*, **10**, 2698.
- Pope, S. B. 1990 (July). Computations of Turbulent Combustion: Progress and Challenges. In: *Twenty Third Symposium (International) on Combustion*.
- Pope, S. B. 2000. *Turbulent Flows*. 1st ed. Cambridge University Press.
- Pope, S. B. 2004. Ten Questions Concerning the Large-Eddy Simulation of Turbulent flows. *New Journal of Physics*, **6**(35), 1–24.
- Porter, D. H., Woodward, P. R., and Pouquet, A. 1998. Inertial Range Structures in Decaying Turbulent Flows. *Physics of Fluids*, **10**(237–245).
- Pullin, D. I. 2000. A Vortex-Based Model for the Subgrid Flux of a Passive Scalar. *Physics of Fluids*, **12**(2311).
- Ramaprabhu, P., Dimonte, G., and Andrews, M. J. 2005. A Numerical Study of the Influence of Initial Perturbations on the Turbulent Rayleigh–Taylor Instability. *Journal of Fluid Mechanics*, **536**, 285–319.
- Reisner, J. M., Josephson, A. J., Gorkowski, K. J., Koo, E., Thompson, D. K., Schroeder, D., and Dubey, M. K. 2023. Informed Multi-Scale Approach Applied to the British Columbia Fires of Late Summer 2017. *Journal of Geophysical Research: Atmospheres*, **128**, e2022JD037238.
- Richardson, L. F. 1927. The Deferred Approach to the Limit. *Trans. R. Soc. London Ser.*, **A226**, 229–361.
- Richtmyer, R. D. 1960. Taylor Instability in Shock Acceleration of Compressible Fluids. *Commun. Pure Appl. Maths.*, **13**, 297–319.
- Ristorcelli, J. R. 2006. Passive Scalar Mixing: Analytic Study of Time Scale Ratio, Variance, and Mix Rate. *Physics of Fluids*, **18**, 1–17.
- Ristorcelli, J. R. 2016. Material Conservation of Passive Scalar Mixing in Finite Scale Navier–Stokes Fluid Turbulence. Chap. 4 of: *Coarse Grained Simulation and Turbulent Mixing*, Grinstein, F. F. (ed). Cambridge University Press.
- Ristorcelli, J. R., Gowardhan, A. A., and Grinstein, F. F. 2013. Two Classes of Richtmyer–Meshkov Instabilities: A Detailed Statistical Look. *Physics of Fluids*, **25**(044106).
- Roache, P. J. 1997. Quantification of Uncertainty in Computational Fluid Dynamics. *Annual Reviews of Fluid Mechanics*, **29**, 123–160.
- Sagaut, P., Deck, S., and Terracol, M. 2006. *Multiscale and Multiresolution Approaches in Turbulence*. Imperial College Press.
- Schiestel, R. 1987. Multiple-Time-Scale Modeling of Turbulent Flows in One-Point Closures. *Physics of Fluids*, **30**(3), 722–731.

- Schilling, O., and Latini, M. 2010. High-Order WENO Simulations of Three-Dimensional Reshocked Richtmyer–Meshkov Instability to Late Times: Dynamics, Dependence on Initial Conditions, and Comparisons to Experimental Data. *Acta Mathematica Scientia*, **30**(2), 595–620.
- Schwarzkopf, J. D., Livescu, D., Baltzer, J. R., Gore, R. A., and Ristorcelli, J. R. 2016. A Two-Length Scale Turbulence Model for Single-Phase Multi-Fluid Mixing. *Flow, Turbulence, and Combustion*, **96**, 1–43.
- Schwarzkopf, J. D., Livescu, D., Gore, R. A., Rauenzahn, R. M., and Ristorcelli, J. R. 2011. Application of a Second-Moment Closure Model to Mixing Processes Involving Multi-Component Miscible Fluids. *Journal of Turbulence*, **49**, 1–35.
- Sessor, M. D., Bond, C. L., and Dimotakis, P. E. 1998. Turbulent Shear-Layer Mixing at High Reynolds Numbers: Effects of Inflow Conditions. *Journal of Fluid Mechanics*, **376**, 115–38.
- Speziale, C. G. 1998. Turbulence Modeling for Time-Dependent RANS and VLES : A Review. *AIAA Journal*, **36**(2), 173–184.
- Sreenivasan, K. R. 1984. On the Scaling of the Turbulence Energy Dissipation Rate. *Physics of Fluids*, **27**(1048).
- Sreenivasan, K. R. 1998. An Update on the Energy Dissipation Rate in Isotropic Turbulence. *Physics of Fluids*, **10**(528).
- Stolz, S., Adams, N. A., and Kleiser, L. 2001. The Approximate Deconvolution Model for Large-Eddy Simulations of Compressible Flows and its Application to Shock-Turbulent-Boundary-Layer Interaction. *Physics of Fluids*, **13**(2985).
- Tennekes, H., and Lumley, J. L. 1972. *A First Course in Turbulence*. MIT Press.
- Thornber, B., Mosedale, A., and Drikakis, D. 2007. On the Implicit Large Eddy Simulation of Homogeneous Decaying Turbulence. *Journal of Computational Physics*, **226**, 1902–1929.
- Thornber, B., Mosedale, A., Drikakis, D., Youngs, D., and Williams, R. J. R. 2008. An Improved Reconstruction Method for Compressible Flows with Low Mach Number Features. *Journal of Computational Physics*, **227**(10), 4873–4894.
- Thornber, B., Drikakis, D., Youngs, D. L., and Williams, R. J. R. 2010. The Influence of Initial Conditions on Turbulent Mixing due to Richtmyer–Meshkov Instability. *Journal of Fluid Mechanics*, **654**, 99–139.
- Toro, E. F., Spruce, M., and Speares, W. 1994. Restoration of the Contact Surface in the HLL-Riemann Solver. *Shock Waves*, **4**(1), 25–34.
- Townsend, A. A. 1976. *Structure of Turbulent Shear Flow*. Cambridge University Press.
- Tsinober, A. 2009. *An Informal Conceptual Introduction to Turbulence*. Springer.
- Tsinober, A. 2011. Models versus Physical Laws, First Principles, or Why Models Work? In: *Workshop at Wolfgang Pauli Institute, Vienna, Austria, 2–4 February*.
- Tsinober, A. 2014. *The Essence of Turbulence as a Physical Phenomenon*. 1st ed. Springer.
- Uranga, A., Persson, P.-O., Drela, M., and Peraire, J. 2011. Implicit Large Eddy Simulation of Transition to Turbulence at Low Reynolds Numbers Using a Discontinuous Galerkin Method. *International Journal for Numerical Methods in Engineering*, **87**, 232–261.
- van Leer, B. 1997. Towards the Ultimate Conservative Difference Scheme. *Journal of Computational Physics*, **135**(2), 229–248.
- Vassilicos, J. C. 2015a. Dissipation in Turbulent Flows. *Annual Review of Fluid Mechanics*, **47**, 95–114.
- Vassilicos, J. C. 2015b. Dissipation in Turbulent Flows. *Annual Review of Fluid Mechanics*, **47**(1), 95–114.
- Verfaillie, S., Gutmark, E. J., Bonnet, J. P., and Grinstein, F. F. 2006. Linear Stochastic Estimation of a Swirling Jet. *AIAA Journal*, **44**, 457–468.
- Visbal, M. R., and Rizzetta, D. P. 2002. Large-Eddy Simulation on Curvilinear Grids Using Compact Differencing and Filtering Schemes. *Journal of Fluids Engineering*, **124**(4), 836–847.
- von Kaenel, R., Adams, N. A., Kleiser, L., and Vos, J. B. 2003. The Approximate Deconvolution Model for Large-Eddy Simulation of Compressible Flows With Finite Volume Schemes. *Journal of Fluids Engineering*, **125**, 375–381.
- Wachtor, A. J., Grinstein, F. F., DeVore, C. R., Ristorcelli, J. R., and Margolin, L. G. 2013. Implicit Large-Eddy Simulation of Passive Scalar Mixing in Statistically Stationary Isotropic Turbulence. *Physics of Fluids*, **25**(025101).
- Wang, R., Wu, F., Xu, H., and Sherwin, S. J. 2021. Implicit Large-Eddy Simulations of Turbulent Flow in a Channel via Spectral/hp Element Methods. *Physics of Fluids*, **33**, 035130.

- Warming, R. F., and Hyett, B. J. 1974. The Modified Equation Approach and the Stability and Accuracy Analysis of Finite-Difference Methods. *Journal of Comp. Phys.*, **14**, 159–179.
- Wynanski, I., Champagne, F., and Marasli, B. 1986. On The Large-Scale Structures In Two-Dimensional, Small-Deficit, Turbulent Wakes. *Journal of Fluid Mechanics*, **168**, 31–71.
- Yao, J., and Hussain, F. 2022. Vortex Reconnection and Turbulence Cascade. *Annual Review of Fluid Mechanics*, **54**, 317–347.
- Yeung, P. K., Xu, S., and Sreenivasan, K. R. 2002. Schmidt Number Effects on Turbulent Transport with Uniform Mean Scalar Gradient. *Physics of Fluids*, **14**, 4178–4191.
- Zhou, Y. 2007. Unification and Extension of the Similarity Scaling Criteria and Mixing Transition for Studying Astrophysics Using High Energy Density Laboratory Experiments or Numerical Simulations. *Physics of Plasmas*, **14**(082701).
- Zhou, Y. 2017a. Rayleigh–Taylor and Richtmyer–Meshkov Instability Induced Flow, Turbulence, and Mixing. I. *Physics Reports*, **720–722**, 1–136.
- Zhou, Y. 2017b. Rayleigh–Taylor and Richtmyer–Meshkov Instability Induced Flow, Turbulence, and Mixing. II. *Physics Reports*, **723–725**, 1–160.
- Zhou, Y., Grinstein, F. F., Wachtor, A. J., and Haines, B. M. 2014. Estimating the Effective Reynolds Number in Implicit Large-Eddy Simulation. *Physical Review E*, **89**(1), 013303.